

---

# Primal-Dual Mesh Convolutional Neural Networks

---

**Francesco Milano\***

ETH Zurich, Switzerland  
fmilano@student.ethz.ch

**Antonio Loquercio**

Robotics and Perception Group  
University of Zurich, Switzerland  
loquercio@ifi.uzh.ch

**Antoni Rosinol**

SPARK Lab  
MIT, USA  
arosinol@mit.edu

**Davide Scaramuzza**

Robotics and Perception Group  
University of Zurich, Switzerland  
sdavide@ifi.uzh.ch

**Luca Carlone**

SPARK Lab  
MIT, USA  
lcarlone@mit.edu

## Abstract

Recent works in geometric deep learning have introduced neural networks that allow performing inference tasks on three-dimensional geometric data by defining convolution –and sometimes pooling– operations on triangle meshes. These methods, however, either consider the input mesh as a graph, and do not exploit specific geometric properties of meshes for feature aggregation and downsampling, or are specialized for meshes, but rely on a rigid definition of convolution that does not properly capture the local topology of the mesh. We propose a method that combines the advantages of both types of approaches, while addressing their limitations: we extend a primal-dual framework drawn from the graph-neural-network literature to triangle meshes, and define convolutions on two types of graphs constructed from an input mesh. Our method takes features for both edges and faces of a 3D mesh as input, and dynamically aggregates them using an attention mechanism. At the same time, we introduce a pooling operation with a precise geometric interpretation, that allows handling variations in the mesh connectivity by clustering mesh faces in a task-driven fashion. We provide theoretical insights of our approach using tools from the mesh-simplification literature. In addition, we validate experimentally our method in the tasks of shape classification and shape segmentation, where we obtain comparable or superior performance to the state of the art.

## 1 Introduction

The development of deep-learning tools that operate on three-dimensional triangular meshes has recently received an increasing attention by the computer graphics, vision, and machine learning communities, due to the availability of large 3D datasets with semantic annotations [1, 2] and to the expressiveness and efficiency of meshes in representing non-uniform, irregular surfaces. Compared to alternative representations often used for 3D geometry, such as voxels and point clouds, that scale poorly to high object resolutions [3], meshes allow representing structure more adaptively and compactly [4]; at the same time, they naturally provide connectivity information, as opposed to point clouds, and lend themselves to simple, commonly used rendering and processing algorithms [5, p. 14]. However, meshes have both a *geometric* and a *topological* component [6, p. 10], represented respectively by the vertices and by the connectivity of edges and faces [5, p. 19]; while the geometrical variability of the underlying surface encodes essential semantic information, the randomness in the discretization of the surface (which can include, e.g., variations in tessellation, isotropy, regularity, *level-of-detail* [5]) is to a certain extent not informative and independent of the

---

\*Work performed while at MIT.

shape identity [7]. This is particularly relevant in the context of shape understanding and semantic-based object representation, where mesh processing requires abstracting from the low-level mesh elements to a higher-level structure-aware representation of the shape [8–10].

Handling 3D geometric data represented as meshes and performing deep learning tasks on them relates to the field of geometric deep learning [11], that attempts to generalize tools from convolutional neural networks (CNNs) to non-Euclidean domains, including graphs and manifolds. Existing methods define specific *convolution* and (optionally) *pooling/unpooling* operations to operate on meshes [12]. We identify two main types of approaches: on the one hand, methods that process the input mesh as a graph [13–16], thus not exploiting important geometrical properties of meshes [17]; on the other hand, *ad-hoc* methods, which design convolution and pooling operations using geometric properties of triangular meshes. However, both types of approaches usually implement a form of *non-dynamic* feature aggregation. Indeed, they learn and apply shared isotropic kernels to all the vertices/edges of the mesh and use a weighting scheme that does not depend on the region of the mesh on which the operation is applied. This is a limiting factor, considering that meshes can exhibit large variations in the density and shape of their faces. Furthermore, graph-based methods often do not perform pooling, or they implement it through generic graph clustering algorithms [18], that do not exploit the mesh geometric characteristics. In contrast, the *ad-hoc* methods that define mesh-specific pooling operations [12] make strong assumptions on the mesh local topology, limiting the number of mesh elements which can be pooled.

**Contributions.** To address the limitations of the approaches above, we propose a method that combines a graph-neural-network framework with mesh-specific insights from *ad-hoc* approaches. Our method, named PD-MeshNet, is the first to perform dynamic, attention-based feature aggregation while also implementing a task-driven, mesh-specific pooling operation. Motivated by the inherent duality between topology and geometry in meshes, we build on the primal-dual graph convolutional framework of [19], and extend it to triangular meshes: starting from an input mesh, we construct two types of graphs, that allow assigning features to both edges and faces of a 3D mesh. The method enables the implementation of *dynamic* feature aggregation –where the relevance of each neighbor in the convolution operation is learned using an attention mechanism [20]– and at the same time allows to learn richer and more complex features [19]. On the other hand, we show that *ad-hoc* methods, such as [12], can be interpreted as an instantiation of our method where only a single graph is considered. Similarly to [12], we also introduce a task-driven pooling operation specific for meshes. A unique feature of our pooling operation, however, is its geometrical interpretation: by collapsing graph edges based on the associated attention coefficients, PD-MeshNet learns to form clusters of faces in the mesh, allowing both to downsample the number of features in the network and to abstract the computation from the low-level, noise-prone mesh elements, to larger areas in the shape. In addition, our pooling operation does not require assumptions on the topological type of the meshes nor has the topological limitations of [12]. We evaluate our method in the tasks of mesh classification and segmentation, where we show results comparable or superior to state-of-the-art approaches. Our code is publicly available at <https://github.com/MIT-SPARK/PD-MeshNet>.

**Notation.** In the following, we assume the reader to be familiar with basic notions from graph theory (*e.g.*, graph embedding,  $k$ -regularity [21, 22]) and meshes (*e.g.*, 1-ring neighborhood, boundary edge/face [5, 6]). We denote the vertices of a generic triangle mesh  $\mathcal{M}$  with lowercase letters (*e.g.*,  $a$ ), and its faces with uppercase letters (*e.g.*,  $A$ ). We refer to the set of all the faces of the mesh as  $\mathcal{F}(\mathcal{M})$ , and we denote the set of the faces adjacent to a generic face  $A \in \mathcal{F}(\mathcal{M})$  as  $\mathcal{N}_A$ . For simplicity and comparability to [12], we assume the mesh  $\mathcal{M}$  to be (*edge-*)*manifold*<sup>2</sup>. However, as we show in the Supplementary Material, our framework allows to relax this assumption and process meshes of any topological type.

## 2 Related Work

**Graph-based methods.** Related to our approach are works that consider meshes as graph-structured data, which is processed by one of the existing variants of graph convolutional networks (GCNs) [23–25, 20, 19]. Some of the methods based on GCNs are specifically designed to work on manifold meshes, whose connectivity allows to define convolution on patches around mesh vertices represented

<sup>2</sup>We recall that a triangle mesh is 2-manifold if its surface is everywhere locally homeomorphic to a disk; in particular, an edge is *non-manifold* if it has more than two incident triangles [6, pp. 11–12].

in an intrinsic coordinate system [13–15]. The above approaches, however, apply shared isotropic kernels to the mesh vertices according to a weighting scheme that is independent of the position on the surface. Therefore, they do not adapt to local variations in the regularity and isotropy of mesh elements. Partially addressing this problem, Verma et al. [16] propose a method that dynamically learns the correspondence between filter weights and neighboring nodes. However, their method implements the pooling operation through a generic graph clustering algorithm [18], which is not aware of the geometry of the mesh. Other graph-based approaches [26] define pooling using classic mesh-simplification techniques for surface approximation [27]. However, the latter algorithm, which approximates the mesh surface by minimizing a geometric error, is not necessarily optimal for the downstream task (*e.g.*, classification or segmentation). In contrast, our approach uses a pooling operation which is both mesh-specific and task-driven. Finally, the recent work of Schult et al. [28] made a step towards addressing dynamic feature aggregation in meshes by proposing to combine a geodesic-based vertex convolution with another convolution on vertices based on Euclidean distance. However, this approach implements pooling through classic mesh-simplification methods that minimize non-task-driven geometric errors [28].

**Ad-hoc methods.** A second class of methods defines convolution and/or pooling by using *ad-hoc* mesh properties [29, 12, 30–33]. Tatarchenko et al. [30] process mesh surfaces with standard 2D convolutions, which operate on feature maps defined on local tangent planes. Similarly, Huang et al. [31] use standard CNNs to extract features from high-resolution texture signals. Feng et al. [29] design a mesh-specific convolution that aggregates spatial and structural features of mesh faces. Hanocka et al. [12] define convolution over edges of the input mesh, which are assumed to be edge-manifold. This assumption allows defining a symmetric convolution operation, which aggregates features from the 1-ring neighborhood of each edge. In addition, it allows pooling according to a task-driven version of the classical *edge-collapse* operation from the mesh-simplification literature [34]. The method of Lim et al. [32], further developed by Gong et al. [33], implements a convolution operation based on *spirals* that are defined around each mesh vertex; this approach, however, requires all the meshes in the dataset to have a similar, fixed, topology. The remaining aforementioned methods, similarly to graph-based approaches, either do not perform *dynamic* aggregation of features [12, 29] or do not provide a mesh-specific downsampling operation [30, 31]. The few exceptions, which define an ad-hoc mesh-pooling operation, *e.g.* [12], make strong assumptions on the topology of the input mesh, *de facto* limiting the number of mesh elements which can be pooled. In contrast, our method performs dynamic feature aggregation through an attention mechanism, and exploits the latter to define a novel pooling operation, tailored to the mesh and the task, which is not limited by the mesh topology.

### 3 PD-MeshNet

This section introduces the building blocks of our method, and in particular the instantiation of the primal-dual graph (Section 3.1), convolution (Section 3.2), and task-driven pooling/unpooling operations (Sections 3.3–3.4).

#### 3.1 Converting 3D Meshes to Graphs

Given an input mesh  $\mathcal{M}$ , PD-MeshNet constructs a primal and a dual graph (Fig. 1).

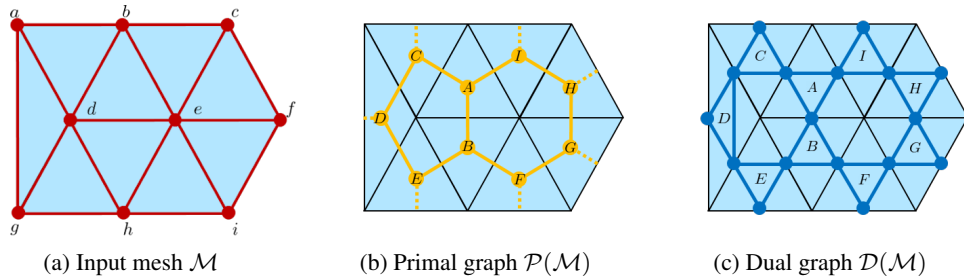


Figure 1: Primal-dual graphs associated to an input mesh in PD-MeshNet. Vertices and faces of the triangle mesh are denoted respectively by lowercase and uppercase letters.

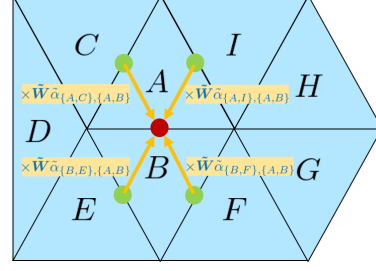
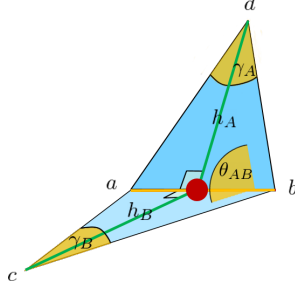


Figure 2: Features of a generic dual node  $\{A, B\}$ : dihedral angle  $\theta_{AB}$ , internal angles  $\gamma_A$  and  $\gamma_B$ , edge-to-height ratios  $\|ab\|/h_A$  and  $\|ab\|/h_B$ . Figure 3: Aggregation of the neighboring features for a generic dual node  $\{A, B\}$  (in red).

The **Primal Graph** of a mesh  $\mathcal{M}$  is an undirected graph having a node for each face of  $\mathcal{M}$  and an edge between two nodes if the corresponding faces are adjacent in  $\mathcal{M}$  (Fig. 1b). We denote our primal graph as  $\mathcal{P}(\mathcal{M})$ . Contrary to related work [13–17], which builds a graph over the mesh vertices, our primal graph operates over the faces of the mesh. The graph built on the mesh vertices – that we denote  $\mathcal{G}(\mathcal{M})$ , and that is visually similar to the one in Fig. 1a – is sometimes called *mesh graph* [3, 16, 17]. On the other hand, a representation akin to the proposed primal graph has been also referred to as *simplex mesh* in related work [35]. By construction, our primal graph  $\mathcal{P}(\mathcal{M})$  is topologically dual of  $\mathcal{G}(\mathcal{M})$  [35, 36]. The advantage of our primal graph is that it allows defining pooling/unpooling operations that can be easily interpreted in terms of clustering of the mesh faces. For each mesh face  $A \in \mathcal{F}(\mathcal{M})$ , we assign to the corresponding node in the primal graph – which we also denote as  $A$  – the feature  $\mathbf{f}_A$ , defined as the ratio between the area of face  $A$  and the sum of the areas of all the faces in  $\mathcal{F}(\mathcal{M})$ .

The **Dual Graph** of a mesh  $\mathcal{M}$  is a graph having a node for each edge  $e \in \mathcal{M}$ , and an edge connecting two nodes where the corresponding mesh edges are adjacent to a face in  $\mathcal{M}$  (Fig. 1c). Interestingly, our dual graph captures the model used in the ad-hoc method of Hanocka et al. [12], which, however, does not explicitly use a graph-based representation. Indeed, as we show in the Supplementary Material, for an edge-manifold triangle mesh  $\mathcal{M}$ , our dual graph  $\mathcal{D}(\mathcal{M})$  (i) is the *line graph* of  $\mathcal{P}(\mathcal{M})$  and (ii) is the *medial graph* of  $\mathcal{G}(\mathcal{M})$ . The dual graph allows performing feature aggregation among edges in a 1-ring neighborhood, which for a manifold triangle mesh is 4-regular (a property exploited in [12]). With such geometric interpretation we take a step forward to bridging the gap between graph-based and ad-hoc methods for mesh processing. This allows our approach to benefit from their respective characteristics.

**Dual Graph Construction.** For each pair of adjacent mesh faces  $A, B \in \mathcal{F}(\mathcal{M})$ , a *single* node  $\{A, B\}$  is created in the dual graph, with undirected edges connecting it to the nodes of the form  $\{A, M\}, M \in \mathcal{N}_A \setminus \{B\}$  and  $\{B, N\}, N \in \mathcal{N}_B \setminus \{A\}$  (cf. Fig. 1c). However, this is not the only viable option to generate the dual graph of the mesh: there are three admissible configurations of the dual graph, which differ in the number of nodes corresponding to each mesh edge and in the directedness of the graph edges. We experimentally noticed minor performance differences by changing the dual graph configuration. In the Supplementary Material we provide more details about these configurations as well as an ablation study of their impact on performance.

**Dual Graph Features.** We assign to each node  $\{A, B\}$  of the dual graph the same type of geometric features as in [12]. Specifically, we use the following features: (i) the dihedral angle  $\theta_{AB}$  between faces  $A$  and  $B$ , (ii) the ratios between the edge shared by  $A$  and  $B$  and the heights of the two faces with respect to the shared edge (edge-to-height ratios), (iii) the internal angles of the two faces. A geometric illustration of these features is presented in Fig. 2.

### 3.2 Convolution

After converting an input 3D mesh to a pair of primal and dual graphs as defined above, we perform the convolution operation using the method of Monti et al. [19], which was previously applied only to graphs from standard graph benchmark datasets [37, 38].

A *primal-dual convolutional layer* consists in the application of two alternating convolution operations on the dual and on the primal graph. In particular, the dual convolutional layer is a graph attention network (GAT) [20]: for a generic dual node  $\{A, B\}$  the layer outputs a feature  $\tilde{\mathbf{f}}'_{\{A, B\}}$  obtained

by aggregating the features of its neighboring nodes  $\{A, M\}$ ,  $M \in \mathcal{N}_A \setminus \{B\}$  and  $\{B, N\}$ ,  $N \in \mathcal{N}_B \setminus \{A\}$ , transformed through a shared learnable kernel  $\tilde{\mathbf{W}}$ . The key property of the approach is that the aggregation is further weighted through *attention coefficients* defined on the edges,  $\{A, M\} \rightarrow \{A, B\}$  and  $\{B, N\} \rightarrow \{A, B\}$  (Fig. 3); for a generic neighboring node  $\{A, M\}$ ,  $M \in \mathcal{N}_A \setminus \{B\}$ , the attention coefficient  $\tilde{\alpha}_{\{A, M\}, \{A, B\}}$  associated to the edge  $\{A, M\} \rightarrow \{A, B\}$  is computed as a variation of the softmax function of the features of  $\{A, B\}$ , of  $\{A, M\}$ , as well as the other neighboring nodes of  $\{A, B\}$ , parameterized by a learnable attention parameter  $\tilde{\mathbf{a}}$ . Similarly, the primal convolution consists of a GAT, with a shared learnable kernel  $\mathbf{W}$  and *primal attention coefficients*  $\alpha_{M, A}$ ,  $M \in \mathcal{N}_A$  defined, for each primal node  $A$ , on the incoming edges of the primal graph. However, since every primal edge has a corresponding node in the dual graph, primal attention coefficients are computed from the dual features; in particular, the attention coefficient  $\alpha_{B, A}$ , associated to the generic primal edge  $B \rightarrow A$ , with  $B \in \mathcal{N}_A$ , is obtained through a variation of the softmax function of the features of the dual node  $\{A, B\}$  and of all the dual nodes of the form  $\{A, M\}$ ,  $M \in \mathcal{N}_A$ , parameterized by a learnable attention parameter  $\mathbf{a}$ . Similarly to [20], multiple versions - also called *heads* - of both the attention parameters  $\tilde{\mathbf{a}}$  and  $\mathbf{a}$  can be used.

### 3.3 Pooling

Our pooling operation consists in an *edge contraction* [21, p. 264] performed in the primal graph  $\mathcal{P}(\mathcal{M})$ . While edge contraction has recently been used also in the graph-neural-network literature to implement pooling on generic graphs [39–41], the unique feature of our approach is the geometric interpretation that this operation has in our framework. Indeed, it is easy to see that an edge contraction in the primal graph  $\mathcal{P}(\mathcal{M})$  corresponds to *merging faces of the mesh*  $\mathcal{M}$  (cf. Fig. 4). This idea was exploited in a classical work in mesh simplification for the purpose of forming *clusters of faces* in meshes [42]. However, while in [42] the edges to be contracted were selected to minimize a

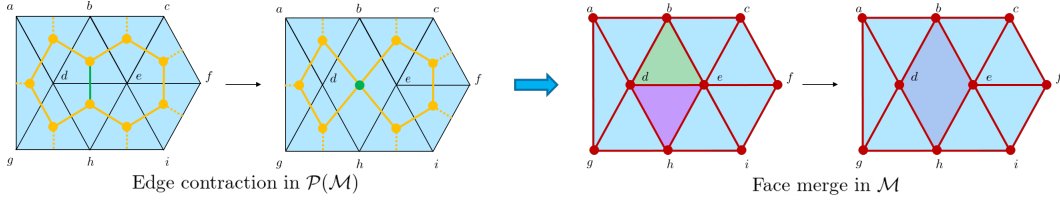


Figure 4: Our pooling operation consists in an attention-driven edge contraction in the primal graph  $\mathcal{P}(\mathcal{M})$ , which corresponds to merging faces of the mesh  $\mathcal{M}$ .

geometric and task-independent error, our approach lets the network *learn* what edges of  $\mathcal{P}(\mathcal{M})$  should be contracted, using the associated primal attention coefficients as a criterion. The key idea of our method is that the attention coefficients between two adjacent primal nodes should encode how *relevant* the information flow between the two corresponding faces of the mesh is, with respect to the task for which the network is trained. This way, by stacking multiple pooling layers PD-MeshNet is able to aggregate feature information over faces and form larger clusters of faces optimized for the task at hand.

More specifically, given two adjacent faces  $A, B \in \mathcal{F}(\mathcal{M})$ , we choose whether to contract the edge between the corresponding primal nodes based on the sum of the attention coefficients along the two directions  $A \rightarrow B$  and  $B \rightarrow A$ , i.e.,

$$\alpha_{A, B} + \alpha_{B, A}. \quad (1)$$

In case multiple attention heads are used, the values (1) from the different heads are averaged. Each pooling layer contracts the  $K$  edges with largest cumulative coefficients (1), where  $K$  is a user-specified parameter<sup>3</sup>; the edges are contracted in parallel. At the output of each pooling layer, the dual graph is efficiently reconstructed on the basis of the pooled primal edges, so as to represent the line graph of the new primal graph<sup>4</sup> (cf. Fig. 5).

We observe that the top- $K$  pooling approach described above allows any two adjacent primal edges to be pooled at the same time, if they are both among the  $K$  edges with the largest quantity (1); indeed,

<sup>3</sup>Equivalently,  $K$  can be expressed as a fraction of the number of primal nodes in the input graph.

<sup>4</sup>It should be noted that after a pooling operation, the dual graph can no longer be interpreted as the medial graph of the  $\mathcal{G}(\mathcal{M})$ . Indeed, the 4-regularity property does not hold anymore (cf. Fig. 5).

in general the operation merges  $n \geq 2$  primal nodes  $A_1, A_2, \dots, A_n$  whose corresponding faces in the mesh form a *triangle fan* [43] into a single primal node, that we denote as  $A_1 A_2 \dots A_n$ .

The feature of the new primal node  $A_1 A_2 \dots A_n$  is determined by summing the features of its constituent nodes  $A_1, A_2, \dots, A_n$ , i.e.,  $f_{A_1 A_2 \dots A_n} := \sum_{i=1}^n f_{A_i}$ . We also considered using averaging as the aggregation function, but empirically found sum-based aggregation to perform slightly better (cf. Supplementary Material for a more detailed comparison).

In general, it is possible that face clusters corresponding to two new adjacent primal nodes shared more than one edge before pooling. Consider, as an example, the case in which the nodes  $A, B$  and the nodes  $C, D, E$  in Fig. 5 were merged into two primal nodes  $AB$  and  $CDE$ , collapsing the edges between  $A$  and  $B$ ,  $C$  and  $D$ , and  $D$  and  $E$ : two primal edges would connect the new primal nodes, corresponding to the dual nodes  $\{A, C\}$  and  $\{B, E\}$  of the original graph.

As shown in Fig. 6, whenever this happens, the two (or more) dual nodes are merged into a single dual node ( $\{AB, CDE\}$  in the example). Similarly to the case of primal nodes, this node is assigned as feature the sum of the features of its constituting nodes. Two other cases are possible for dual graphs when a primal edge is contracted: (i) a dual node is removed from the graph, when the corresponding primal edge is contracted, (ii) a dual node is kept in the graph with the same feature, if it is the only dual node that corresponds to an edge between two new primal nodes.

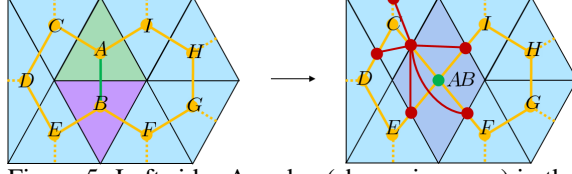


Figure 5: Left side: An edge (shown in green) in the primal graph (depicted in yellow) is contracted. Right side: the dual graph is updated so as to match the line graph of the new primal graph. As an example, shown in red is the new dual node  $\{AB, C\}$  with its neighborhood in the updated dual graph.

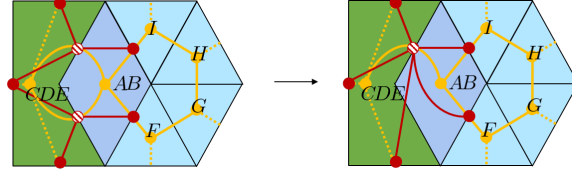


Figure 6: Collapsing primal edges  $A-B$ ,  $C-D$ , and  $D-E$  in the left side of Fig. 5 causes two existing dual nodes (striped on the left side) to correspond to primal edges between the same two new primal nodes  $AB$  and  $CDE$ . The two dual nodes get merged into a single one (striped on the right side).

We finally note that the edge collapse operation used in [12] suffers from a topological limitation: collapsing a mesh edge which is adjacent to a valence-3 vertex is not allowed, as it would cause the formation of a non-manifold edge [44], breaking the required assumption of edge manifoldness (cf. Sec. C.1 of the Supplementary Material). In practice, this limits the number of edges that can be pooled, and consequently poses a restriction to the resolution that can be reached through the downsampling operation. On the contrary, our pooling method has no such limitations (in principle, it would be possible to obtain a single face cluster for each connected component in the mesh [42]), and has the further advantage of allowing at any time to map an element (face) in the original mesh to the corresponding face cluster in the simplified mesh.

### 3.4 Unpooling

As we show in the next section, the experiments performed on mesh segmentation tasks rely on an encoder-decoder architecture, and thus require implementing an unpooling operation. To achieve this, we simply store the connectivity of the primal and dual graphs at the input of each pooling layer, and we use look-up operations to restore it in the unpooling layers, which are in 1-to-1 correspondence with the pooling layers. Therefore, the operation maps larger face clusters to smaller ones; both the primal and the dual nodes associated to the smaller clusters are assigned the same features as the corresponding nodes in the larger clusters. Due to the fact that a pooling operation may remove some dual nodes (cf. Section 3.3), in general some nodes in the dual graph outputted by the unpooling layer will not have a corresponding node in the input dual graph; we learn a single parameter vector that we assign as feature to all such nodes.

## 4 Experiments

We evaluate PD-MeshNet on the tasks of mesh classification and mesh segmentation. On these tasks and on several datasets, we outperform start-of-the-art methods. In all the experiments we use Adam algorithm [45] for optimization. We implement our framework in PyTorch [46], using the geometric-deep-learning library PyTorch Geometric [47].

### 4.1 Shape Classification

The goal of shape classification is to assign each input mesh to a category (*e.g.*, chair, table). For the experiments on this task, we use a simple architecture consisting of a two stacked residual blocks, each containing two *primal-dual convolutional layers* and each attached to a pooling layer at its output. Similarly to [12], we insert a global average pooling layer after the last pooling layer, and we apply it on the features of the dual graph. The output of the average pooling layer is processed by a two-layer perceptron with ReLU activation, which predicts the class label for the input mesh. The network is trained using cross-entropy on the predicted labels. We do not perform any form of data augmentation. Additional details on the architecture parameters may be found in the Supplementary Material.

**SHREC dataset.** We use the lower-resolution version of the SHREC dataset [48] provided by [12], which consists of watertight meshes with 750 edges and 500 faces each. The dataset is made up of 600 samples from 30 different classes, with each class containing 20 samples.

Similarly to [12], we perform the evaluation on two types of dataset splits: *split 16* – where for each class 16 samples are used for training and 4 for testing – and *split 10* – in which the samples of each class are subdivided equally between training and the test set.

Following the same setup as [12], we limit the number of training epochs to 200, and for both *split 16* and *split 10* we randomly generate 3 sets and average our results over them. Table 1 shows that our method outperforms [12] by 4.6% on average over the splits. In addition, we also outperform the other baselines, which are volumetric and based on geometry images, by up to 36.5%.

Method	Split 16	Split 10
Ours	<b>99.7%</b>	<b>99.1%</b>
MeshCNN [12]	98.6%	91.0%
GWCNN [49]	96.6%	90.3%
GI [50]	96.6%	88.6%
SN [51]	48.4%	52.7%
SG [52]	70.8%	62.6%

Table 1: Classification accuracy on test set, SHREC dataset (comparisons from [12]).

**Cube Engraving dataset.** A second mesh-classification experiment is conducted on Cube Engraving dataset released by [12], which was generated using samples from the *MPEG-7* binary shape [53] dataset and inseting them into cubes with random position and orientation. Therefore, achieving good performance on this dataset requires learning distinctive features of the inset objects while neglecting the uninformative faces of the cubes.

The dataset consists of objects engraved in cubes and distributed in 22 classes with 200 samples per class (170 training samples and 30 test samples). Table 2 shows the results of this evaluation, in which our approach improves the accuracy by 2.23% with respect to the baseline of Hanocka et al. [12] and by 30.13% with respect to the point-cloud based PointNet++ [54].

Method	Test accuracy
Ours	<b>94.39%</b>
MeshCNN [12]	92.16%
PointNet++ [54]	64.26%

Table 2: Classification accuracy on test set, Cube Engraving dataset (comparisons from [12]).

### 4.2 Shape Segmentation

We evaluate our approach also on the task of shape segmentation, which consists in predicting a class label for each element (face, vertex, or edge) of a given mesh. In particular, since our method naturally aggregates information on clusters of faces, we predict a class label for each mesh face. Similarly to [12], we use a U-Net [55] encoder-decoder architecture with skip connections. The encoder is formed of 3 residual blocks with convolution layers, each followed by pooling. The decoder consists of 3 unpooling layers, each followed by a convolutional layer. The output of the network is a pair



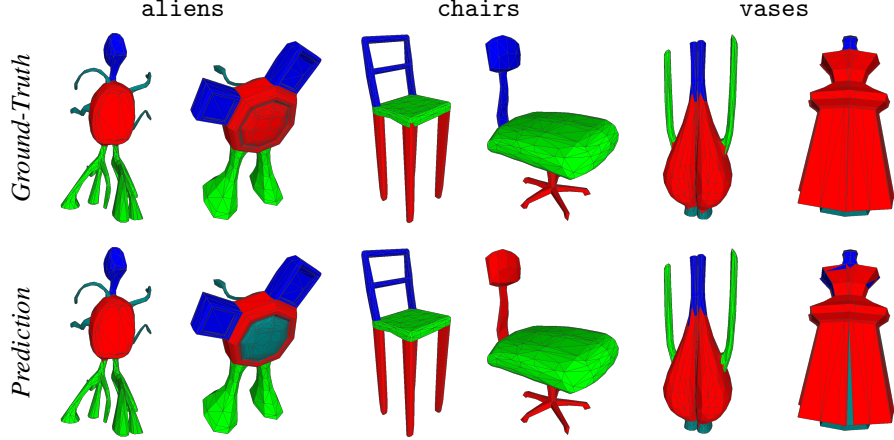


Figure 7: Example segmentations from the COSEG dataset. Same color corresponds to same class label. Due to its ability to create hierarchical clusters of faces, our approach predicts very accurate segmentations. The main failure case of our method consists in associating clusters to the wrong category.

of primal/dual graphs in the original input resolution. Every node of the resulting primal graph (uniquely associated to one of the input mesh faces) is associated with a per-class score, which is trained using cross-entropy loss for 1000 epochs. We perform experiments on two benchmarks for the task: COSEG [56] and Human Body [57]. Since these datasets contain ground-truth labels on the mesh edges, we convert the edge annotations into per-face labels by majority voting, selecting for each face the class label that is assigned to most edges in the face.

**Metrics.** Since our method and [12] are trained with labels on different mesh elements (faces and edges, respectively) performing a fair comparison for the shape segmentation task is challenging. As our method is trained on mesh faces, we measure performance according to the percentage of correctly-labelled mesh faces (*Face labels*). In order to compare with [12], we convert the edge labels predicted by the latter into face labels using the same procedure used to generate ground-truth, based on majority-voting. To ensure a fair comparison, in the very few cases (approximately 0.3%  $\sim$  0.7% of the total) in which [12] predicts 3 different labels for the edges of a face, we do not consider the face in the evaluation. For reference, we also report the classification accuracy obtained by Hanocka et al. [12] on edge labels, which the method is trained on (*Edge labels*). This accuracy requires predicting a single label for each mesh edge, therefore a direct comparison with our method on this metric is not possible, since this would require converting per-face labels to per-edge single labels. However, we provide a more extensive analysis of the metrics in Sec. H of the Supplementary Material, where we perform comparisons also according to edge-based metrics and show that our method outperforms [12] also on these types of accuracies. We rerun each of the experiments of [12] 4 times – using the official code and parameters provided – and we report the best accuracy obtained.

**COSEG Dataset.** For evaluation we use the same dataset splits as [12]. The input meshes are divided into the following three categories, for each of which a different experiment is performed:

- Category *aliens*, consisting of 198 samples (169 training set, 29 test set) with 4 class labels;
- Category *chairs*, that contains 397 samples (337 training set, 60 test set) with 3 class labels;
- Category *vases*, made of 297 samples (252 training set, 45 test set) with 4 class labels.

Table 3 compares the results obtained by our method and by [12] on the three categories in the COSEG dataset, using the metrics defined above. For the metric on face labels our method outperforms [12] by up to 4.24%. We believe this performance boost to be motivated by the way our approach aggregates information across faces, which allows to identify structurally coherent clusters in a mesh more naturally than methods based on collapsing mesh edges. This is qualitatively illustrated in Fig. 7, where we show that our method produces high-quality segmentation masks. Fig. 8 further shows that the cluster of faces formed through the attention-driven pooling operation indeed tend to abstract to larger areas which carry common semantic information; we stress that the network does not always find such structures, but also highlight that no supervision on the face clusters was provided during training.



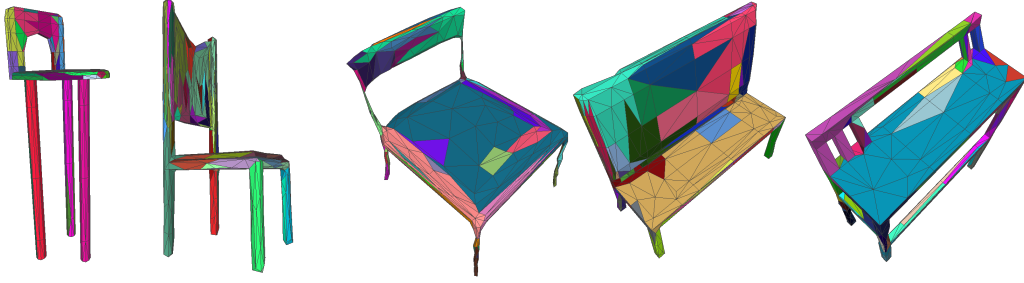


Figure 8: Example of clusters internally formed by PD-MeshNet on samples from the COSEG chair dataset; same color corresponds to same cluster. The clusters shown are outputted by the last pooling layer in the network (cf. Supplementary Material for further details on the architecture). On the left, the legs of the chairs are consistently identified as clusters; on the right, larger common planar structures are found across different samples.

Category	Method	Metric	
		Edge labels	Face labels
aliens	MeshCNN [12]	95.35%	96.26%
	Ours	-	<b>98.18%</b>
chairs	MeshCNN [12]	92.65%	92.99%
	Ours	-	<b>97.23%</b>
vases	MeshCNN [12]	91.96%	92.38%
	Ours	-	<b>95.36%</b>

Table 3: Test accuracy on mesh segmentation task, COSEG dataset.

Method	Metric	
	Edge labels	Face labels
MeshCNN [12]	84.05%	85.39%
Ours	-	<b>85.61%</b>

Table 4: Test accuracy on mesh segmentation task, Human Body dataset.

**Human Body Dataset.** The dataset consists of 381 training samples and 18 test samples, both with a resolution of 1500 faces. Similarly to Hanocka et al. [12], we generate 20 augmented versions of each training sample by randomly shifting the vertices along the edges. As shown in Table 4, also in this dataset our approach outperforms the baseline. However, the performance gap is lower than for the other experiment.

## 5 Conclusions

In this paper, we presented PD-MeshNet, a novel deep-learning framework for processing 3D meshes. Our approach combines an attention-based convolution operation on two graphs constructed from an input 3D mesh with a task-driven pooling operation that corresponds to clustering mesh faces. We achieve a performance superior or comparable to the state-of-the-art on the tasks of shape segmentation and shape classification. Our method is the first to create a connection between graph-based and ad-hoc methods for mesh processing. We believe that further developing this connection is an interesting avenue for future work.

We empirically noticed a performance drop when the network gets too deep (due to the larger number of parameters associated with the two graphs and the more complex optimization landscape), a problem shared by graph neural networks in general [58, 59]. Moreover, pooling layers can be sensitive to their threshold parameters, with too-aggressive a pooling causing a degradation of results. Addressing these limitations is an interesting direction for future work.

Finally, we believe that the higher-level abstraction suggested by our pooling operation could set the basis for a hierarchical representation of objects and, subsequently, scenes. Such representation would be beneficial to all applications requiring a high-level semantic understanding of the environment.

## Broader Impact

Processing of 3D data, in the form of point-cloud, voxel-grids, or meshes finds important applications in several fields, including computer graphics, vision, and robotics. Further developments of this work, which proposes a novel framework for mesh processing based on deep learning, could have a benefit on several real-world applications, including augmented and virtual reality, robotics, and spatial 3D scene understanding of environments. These applications can have profound positive implications for the future of our society, by, for example, improving the quality of virtual social interactions, or increasing the spatial-awareness of current robotic systems to integrate them in our everyday life.

## Acknowledgments and Disclosure of Funding

This work was partially funded by ARL DCIST CRA W911NF-17-2-0181, and MIT Lincoln Laboratory “Task Execution with Semantic Segmentation” program. This work was also partially supported by the National Centre of Competence in Research (NCCR) Robotics through the Swiss National Science Foundation (SNSF) and the SNSF-ERC Starting Grant. Francesco Milano was partially supported by the Zeno Karl Schindler Foundation Master Thesis Grant.

## References

- [1] A. Dai, A. X. Chang, M. Savva, M. Halber, T. Funkhouser, and M. Nießner, “ScanNet: Richly-annotated 3D Reconstructions of Indoor Scenes,” in *IEEE Conf. on Computer Vision and Pattern Recognition (CVPR)*, 2017.
- [2] A. Chang, A. Dai, T. Funkhouser, M. Halber, M. Niessner, M. Savva, S. Song, A. Zeng, and Y. Zhang, “Matterport3D: Learning from RGB-D Data in Indoor Environments,” in *Intl. Conf. on 3D Vision (3DV)*, 2017.
- [3] E. Smith, S. Fujimoto, A. Romero, and D. Meger, “GEOMETRICS: Exploiting Geometric Structure for Graph-Encoded Objects,” in *Intl. Conf. on Machine Learning (ICML)*, 2019.
- [4] L. Gao, J. Yang, T. Wu, Y.-J. Yuan, H. Fu, Y.-K. Lai, and H. Zhang, “SDM-NET: Deep Generative Network for Structured Deformable Mesh,” in *ACM SIGGRAPH Conf. and Exhibition on Computer Graphics and Interactive Techniques in Asia (SIGGRAPH Asia)*, 2019.
- [5] D. P. Luebke, M. Reddy, J. D. Cohen, A. Varshney, B. Watson, and R. Huebner, *Level of Detail for 3D Graphics*. Morgan Kaufmann, 2003.
- [6] M. Botsch, L. Kobbelt, M. Pauly, P. Alliez, and B. Levy, *Polygon Mesh Processing*. A K Peters/CRC Press, 2010.
- [7] I. Kostrikov, Z. Jiang, D. Panozzo, D. Zorin, and J. Bruna, “Surface Networks,” in *IEEE Conf. on Computer Vision and Pattern Recognition (CVPR)*, 2018.
- [8] A. Shamir, “A survey on Mesh Segmentation Techniques,” *Computer Graphics Forum*, vol. 27, no. 6, p. 1539–1556, 2008.
- [9] M. Attene, B. Falcidieno, and M. Spagnuolo, “Hierarchical mesh segmentation based on fitting primitives,” *The Visual Computer*, vol. 22, no. 3, pp. 181–193, 2016.
- [10] N. J. Mitra, M. Wand, H. Zhang, D. Cohen-Or, and M. Bokeloh, “Structure-Aware Shape Processing,” in *ACM SIGGRAPH Intl. Conf. on Computer Graphics and Interactive Techniques (SIGGRAPH)*, 2014.
- [11] M. M. Bronstein, J. Bruna, Y. LeCun, A. Szlam, and P. Vandergheynst, “Geometric deep learning: going beyond Euclidean data,” *Signal Processing Magazine*, vol. 34, no. 4, pp. 18–42, 2017.
- [12] R. Hanocka, A. Hertz, N. Fish, R. Giryes, S. Fleishman, and D. Cohen-Or, “MeshCNN: A Network with an Edge,” *ACM Trans. Graph.*, vol. 38, no. 4, p. 90, 2019.
- [13] J. Masci, D. Boscaini, M. M. Bronstein, and P. Vandergheynst, “Geodesic convolutional neural networks on Riemannian manifolds,” in *Intl. Conf. on Computer Vision (ICCV)*, 2015.
- [14] D. Boscaini, J. Masci, E. Rodolà, and M. M. Bronstein, “Learning shape correspondence with anisotropic convolutional neural networks,” in *Advances in Neural Information Processing Systems (NIPS)*, 2016.

- [15] F. Monti, D. Boscaini, J. Masci, E. Rodolà, J. Svoboda, and M. M. Bronstein, “Geometric deep learning on graphs and manifolds using mixture model CNNs,” in *IEEE Conf. on Computer Vision and Pattern Recognition (CVPR)*, 2017.
- [16] N. Verma, E. Boyer, and J. Verbeek, “FeaStNet: Feature-Steered Graph Convolutions for 3D Shape Analysis,” in *IEEE Conf. on Computer Vision and Pattern Recognition (CVPR)*, 2018.
- [17] P. de Haan, M. Weiler, T. Cohen, and M. Welling, “Gauge Equivariant Mesh CNNs: Anisotropic convolutions on geometric graphs,” *CoRR abs/2003.05425*, 2020.
- [18] I. S. Dhillon, Y. Guan, and K. Brian, “Weighted Graph Cuts without Eigenvectors: A Multilevel Approach,” *IEEE Trans. Pattern Anal. Machine Intell.*, vol. 29, no. 11, pp. 1944–1957, 2007.
- [19] F. Monti, O. Shchur, A. Bojchevski, O. Litany, S. Günnemann, and M. M. Bronstein, “Dual-Primal Graph Convolutional Networks,” in *European Conf. on Machine Learning and Principles and Practice of Knowledge Discovery in Databases (ECML-PKDD)*, 2018.
- [20] P. Veličković, G. Cucurull, A. Casanova, A. Romero, P. Liò, and Y. Bengio, “Graph Attention Networks,” in *Intl. Conf. on Learning Representations (ICLR)*, 2018.
- [21] J. L. Gross and J. Yellen, *Handbook of Graph Theory*. CRC Press, 2003.
- [22] B. Bollobas, *Modern Graph Theory*. Springer, 2013, ch. X, p. 368.
- [23] T. N. Kipf and M. Welling, “Semi-Supervised Classification with Graph Convolutional Networks,” in *Intl. Conf. on Learning Representations (ICLR)*, 2017.
- [24] M. Defferrard, X. Bresson, and P. Vandergheynst, “Convolutional Neural Networks on Graphs with Fast Localized Spectral Filtering,” in *Advances in Neural Information Processing Systems (NIPS)*, 2016.
- [25] M. Simonovsky and N. Komodakis, “Dynamic Edge-Conditioned Graph Convolutional Network,” in *IEEE Conf. on Computer Vision and Pattern Recognition (CVPR)*, 2017.
- [26] A. Ranjan, T. Bolkart, S. Sanyal, and M. J. Black, “Generating 3D faces using Convolutional Mesh Autoencoders,” in *European Conf. on Computer Vision (ECCV)*, 2018.
- [27] M. Garland and P. S. Heckbert, “Surface Simplification using Quadric Error Metrics,” in *ACM SIGGRAPH Intl. Conf. on Computer Graphics and Interactive Techniques (SIGGRAPH)*, 1997.
- [28] J. Schult, F. Engelmann, T. Kontogianni, and B. Leibe, “DualConvMesh-Net: Joint Geodesic and Euclidean Convolutions on 3D Meshes,” *CoRR abs/2004.01002*, 2020.
- [29] Y. Feng, Y. Feng, H. You, X. Zhao, and Y. Gao, “MeshNet: Mesh Neural Network for 3D Shape Representation,” in *AAAI Conf. on Artificial Intelligence (AAAI)*, 2019.
- [30] M. Tatarchenko, J. Park, V. Koltun, and Q.-Y. Zhou, “Tangent Convolutions for Dense Prediction in 3D,” in *IEEE Conf. on Computer Vision and Pattern Recognition (CVPR)*, 2018.
- [31] J. Huang, H. Zhang, L. Yi, T. Funkhouser, M. Niessner, and L. J. Guibas, “TextureNet: Consistent Local Parametrizations for Learning From High-Resolution Signals on Meshes,” in *IEEE Conf. on Computer Vision and Pattern Recognition (CVPR)*, 2019.
- [32] I. Lim, A. Dielen, M. Campen, and L. Kobbelt, “A Simple Approach to Intrinsic Correspondence Learning on Unstructured 3D Meshes,” 2018.
- [33] S. Gong, L. Chen, M. Bronstein, and S. Zafeiriou, “SpiralNet++: A Fast and Highly Efficient Mesh Convolution Operation,” 2019.
- [34] H. Hoppe, T. DeRose, T. Duchamp, J. McDonald, and W. Stuetzle, “Mesh Optimization,” in *ACM SIGGRAPH Intl. Conf. on Computer Graphics and Interactive Techniques (SIGGRAPH)*, 1993.
- [35] H. Delingette, “Simplex Meshes: a General Representation for 3D Shape Reconstruction,” INRIA, Tech. Rep. 2214, Mar 1994.
- [36] —, “General Object Reconstruction Based on Simplex Meshes,” *Intl. J. of Computer Vision*, vol. 32, no. 2, pp. 111–146, 1999.
- [37] A. K. McCallum, K. Nigam, J. Rennie, and K. Seymore, “Automating the Construction of Internet Portals with Machine Learning,” *Information Retrieval*, vol. 3, no. 2, pp. 127 – 163, 2000.

- [38] P. Sen, G. Namata, M. Bilgic, L. Getoor, B. Galligher, and T. Eliassi-Rad, “Collective classification in network data,” *AI Magazine*, vol. 29, no. 3, pp. 93 – 106, 2008.
- [39] F. Diehl, T. Brunner, M. Truong-Le, and A. Knoll, “Towards Graph Pooling by Edge Contraction,” in *Intl. Conf. on Machine Learning (ICML), Workshop on Learning and Reasoning with Graph-Structured Representations*, 2019.
- [40] J. Lee, I. Lee, and J. Kang, “Self-Attention Graph Pooling,” in *Intl. Conf. on Machine Learning (ICML)*, 2019.
- [41] H. Gao and S. Ji, “Graph U-Nets,” in *Intl. Conf. on Machine Learning (ICML)*, 2019.
- [42] M. Garland, A. Willmott, and P. S. Heckbert, “Hierarchical Face Clustering on Polygonal Surfaces,” in *ACM Sym. on Interactive 3D Graphics (I3D)*, 2001, pp. 49–58.
- [43] Ø. Hjelle and M. Dæhlen, *Triangulations and Applications*, ser. Mathematics and Visualization. Springer Berlin Heidelberg, 2006, p. 40.
- [44] T. Dey, H. Edelsbrunner, S. Guha, and D. V. Nekhayev, “Topology Preserving Edge Contraction,” *Publications de l’Institut Mathématique*, vol. 66, no. 80, pp. 23–45, 1999.
- [45] D. P. Kingma and J. Lei Ba, “Adam: A Method for Stochastic Optimization,” in *Intl. Conf. on Learning Representations (ICLR)*, 2015.
- [46] A. Paszke, S. Gross, F. Massa, A. Lerer, J. Bradbury, G. Chanan, T. Killeen, Z. Lin, N. Gimelshein, L. Antiga, A. Desmaison, A. Kopf, E. Yang, Z. DeVito, M. Raison, A. Tejani, S. Chilamkurthy, B. Steiner, L. Fang, J. Bai, and S. Chintala, “PyTorch: An Imperative Style, High-Performance Deep Learning Library,” in *Advances in Neural Information Processing Systems (NeurIPS)*, 2019.
- [47] M. Fey and J. E. Lenssen, “Fast Graph Representation Learning with PyTorch Geometric,” in *ICLR Workshop on Representation Learning on Graphs and Manifolds*, 2019.
- [48] Z. Lian, A. Godil, B. Bustos, M. Daoudi, J. Hermans, S. Kawamura, Y. Kurita, G. Lavoua, H. Nguyen, R. Ohbuchi, Y. Ohikita, Y. Ohishi, F. Porikli, M. Reuter, I. Sipiran, D. Smeets, P. Suetens, H. Tabia, and D. Vandermeulen, “Shape Retrieval on Non-rigid 3D Watertight Meshes,” in *Eurographics Workshop on 3D Object Retrieval*, 2011.
- [49] D. Ezuz, J. Solomon, V. G. Kim, and M. Ben-Chen, “GWCNN: A Metric Alignment Layer for Deep Shape Analysis,” *Eurographics Sym. on Geometry Processing*, vol. 36, no. 5, 2017.
- [50] A. Sinha, J. Bai, and K. Ramani, “Deep Learning 3D Shape Surfaces Using Geometry Images,” in *European Conf. on Computer Vision (ECCV)*, 2016.
- [51] Z. Wu, S. Song, A. Khosla, F. Yu, L. Zhang, X. Tang, and J. Xiao, “3D ShapeNets: A deep representation for volumetric shapes,” in *IEEE Conf. on Computer Vision and Pattern Recognition (CVPR)*, 2015.
- [52] A. M. Bronstein, M. M. Bronstein, L. J. Guibas, and M. Ovsjanikov, “Shape google: Geometric words and expressions for invariant shape retrieval,” *ACM Trans. Graph.*, vol. 30, no. 1, p. 1, 2011.
- [53] L. Latecki and R. Lakamper, “Shape similarity measure based on correspondence of visual parts,” *IEEE Trans. Pattern Anal. Machine Intell.*, vol. 22, no. 10, pp. 1185 – 1190, 2000.
- [54] C. R. Qi, L. Yi, H. Su, and L. J. Guibas, “PointNet++: Deep Hierarchical Feature Learning on Point Sets in a Metric Space,” in *Advances in Neural Information Processing Systems (NIPS)*, 2017.
- [55] O. Ronneberger, P. Fischer, and T. Brox, “U-Net: Convolutional Networks for Biomedical Image Segmentation,” in *Intl. Conf. on Medical Image Computing and Computer Assisted Intervention (MICCAI)*, 2015.
- [56] Y. Wang, S. Asafi, O. van Kaick, H. Zhang, D. Cohen-Or, and B. Chen, “Active co-analysis of a set of shapes,” *ACM Trans. Graph.*, vol. 31, no. 6, p. 165, 2012.
- [57] H. Maron, M. Galun, N. Aigerman, M. Trope, N. Dym, E. Yumer, V. G. Kim, and Y. Lipman, “Convolutional Neural Networks on Surfaces via Seamless Toric Covers,” *ACM Trans. Graph.*, vol. 36, no. 4, p. 71, 2017.
- [58] Q. Li, Z. Han, and X.-M. Wu, “Deeper Insights into Graph Convolutional Networks for Semi-Supervised Learning,” in *AAAI Conf. on Artificial Intelligence (AAAI)*, 2018.
- [59] G. Li, M. Müller, A. Thabet, and B. Ghanem, “DeepGCNs: Can GCNs Go as Deep as CNNs?” in *Intl. Conf. on Computer Vision (ICCV)*, 2019.

---

# Supplementary Material of Primal-Dual Mesh Convolutional Neural Networks

---

**Francesco Milano\***  
ETH Zurich, Switzerland  
fmilano@student.ethz.ch

**Antonio Loquercio**  
Robotics and Perception Group  
University of Zurich, Switzerland  
loquercio@ifi.uzh.ch

**Antoni Rosinol**  
SPARK Lab  
MIT, USA  
arosinol@mit.edu

**Davide Scaramuzza**  
Robotics and Perception Group  
University of Zurich, Switzerland  
sdavide@ifi.uzh.ch

**Luca Carlone**  
SPARK Lab  
MIT, USA  
lcarlone@mit.edu

## Contents

<b>A</b>	<b>Classification of related work</b>	<b>3</b>
A.1	Forms of dynamic aggregation . . . . .	3
<b>B</b>	<b>Analogy between line graph and medial graph</b>	<b>3</b>
<b>C</b>	<b>Further details on graphs</b>	<b>4</b>
C.1	Handling non-manifoldness . . . . .	4
C.2	Dual-graph features . . . . .	5
C.3	Dual-graph configurations . . . . .	5
C.4	Ablation study . . . . .	6
<b>D</b>	<b>Further details on convolution</b>	<b>7</b>
D.1	Dual convolution . . . . .	7
D.1.1	Dual-graph configuration <b>A</b> . . . . .	7
D.1.2	Dual-graph configuration <b>B</b> . . . . .	8
D.1.3	Dual-graph configuration <b>C</b> . . . . .	8
D.2	Primal convolution . . . . .	8
<b>E</b>	<b>Further details on pooling</b>	<b>9</b>
E.1	Implementation details . . . . .	9
<b>F</b>	<b>Architectures and training details</b>	<b>9</b>
F.1	Classification . . . . .	9

---

\*Work performed while at MIT.

F.2 Segmentation . . . . .	10
<b>G Ablation study on components</b>	<b>13</b>
<b>H Metrics</b>	<b>13</b>
<b>I Runtime</b>	<b>15</b>



## A Classification of related work

Table A.1 summarizes the most relevant related works that perform learning-based processing of meshes. Each method is classified according to the type of approach (graph-based/non-graph-based), to the type of pooling (no pooling, mesh-based/non-mesh-based, task-driven/non-task-driven), to the implementation of a form of dynamic feature aggregation, and to the type of task for which the method is designed.

Method	Type of method		Pooling			Dynamic aggr.	Task	
	Graph-based		Non-graph	Non-mesh based	Mesh-based			
	Spatial	Spectral			Non-task-driven			Task-driven
GCNN [1]	✗						Shape correspondence	
ACNN [2]	✗						Shape correspondence/description/retrieval	
MoNet [3]	✗						Shape correspondence	
FeaStNet [4]	✗			✗ ([5])		✗	Shape correspondence/segmentation	
GEM-CNN [6]	✗						Shape correspondence/classification	
DCM-Net [7]	✗ ([8])				✗ ([9]/[10])	✗	Scene segmentation	
SN [11]		✗					Deformation prediction/generative model	
CoMA [12]		✗			✗ ([9])		Generative model	
TangentConv [13]			✗	✗ (grid-based)			Scene segmentation	
TextureNet [14]			✗	✗ (sample-based)			Scene segmentation	
MeshCNN [15]			✗			✗	Shape classification/segmentation	
MeshNet [16]			✗				Shape classification/retrieval	
SyncSpecCNN [17]		✗		✗ (spectral)			Shape segmentation/keypoint prediction	
SpiralNet++ [18]	✗				✗ ([9])	✗	Shape correspondence/classification/reconstruction	
PD-MeshNet	✗					✗	Shape classification/segmentation	

Table A.1: Classification of most relevant related work that perform learning-based processing of meshes.

### A.1 Forms of dynamic aggregation

For each node in an input graph, FeaStNet [4] dynamically learns the correspondence between its neighboring nodes and the filter weights based on the features of the node and of its neighbors. DCM-Net [7] dynamically determines the neighbors of each node in its convolution based on Euclidean distance.

## B Analogy between line graph and medial graph

In the following, we show that, for an edge-manifold, triangle mesh  $\mathcal{M}$ , the medial graph of the mesh graph  $\mathcal{G}(\mathcal{M})$  coincides with the line graph of the primal graph, *i.e.*,  $M(\mathcal{G}(\mathcal{M})) \equiv \mathcal{L}(\mathcal{P}(\mathcal{M}))$  (cf. Theorem 1). For simplicity, we further assume the mesh to be of genus 0; a similar result can be obtained for embeddings on surfaces of higher genus by extending Lemma 2. For convenience, we report here the definitions of *line graph* and *medial graph*:

- The *line graph*  $\mathcal{L}(G)$  of a graph  $G$  has a node for each edge of  $G$ , and two nodes in  $\mathcal{L}(G)$  are adjacent if and only if the corresponding edges in  $G$  have a node in common [19, p. 20].
- The *medial graph*  $M(G)$  of a *plane* graph  $G$  - or more generally of a graph embedded on a higher-genus surface [19, p. 723] - has a node for each edge of  $G$  and an edge between two nodes if the edges of  $G$  corresponding to the two nodes are adjacent on one face of  $G$  [20].

**Assumption 1.**  $\mathcal{M}$  is an edge-manifold, triangle mesh of genus 0.

**Lemma 1.** Under Assumption 1,  $\mathcal{P}(\mathcal{M})$  is a cubic (*i.e.*, 3-regular), planar graph.

*Proof.* 3-regularity follows by definition of simplex mesh, together with the fact that  $\mathcal{M}$  is triangular by hypothesis. The further hypothesis of edge-manifoldness yields the fact that  $\mathcal{P}(\mathcal{M})$  is a planar graph, by definition of edge-manifoldness.  $\square$

**Lemma 2** (Ore [21]). *The medial graph of a cubic plane graph coincides with its line graph.*

**Corollary 1.**  $M(\mathcal{P}(\mathcal{M})) \equiv \mathcal{L}(\mathcal{P}(\mathcal{M}))$ .

*Proof.* The proposition follows directly from Lemmas 1 and 2.  $\square$

**Lemma 3** (Gross and Yellen [19, p. 724]). *The medial graph of a plane graph – and more generally of a graph embedded on a surface – is identical to the medial graph of its dual graph.*

**Theorem 1.**  $M(\mathcal{G}(\mathcal{M})) \equiv \mathcal{L}(\mathcal{P}(\mathcal{M}))$ .

*Proof.* By definition, our primal graph  $\mathcal{P}(\mathcal{M})$  is the (topologically) dual graph of  $\mathcal{G}(\mathcal{M})$  [22], hence  $M(\mathcal{G}(\mathcal{M})) \equiv M(\mathcal{P}(\mathcal{M}))$  from Lemma 3. From Corollary 1 it also holds that  $M(\mathcal{P}(\mathcal{M})) \equiv \mathcal{L}(\mathcal{P}(\mathcal{M}))$ ; thus,  $M(\mathcal{G}(\mathcal{M})) \equiv \mathcal{L}(\mathcal{P}(\mathcal{M}))$ .  $\square$

## C Further details on graphs

### C.1 Handling non-manifoldness

In the following, we show that PD-MeshNet can be easily extended to handle non-manifold meshes. The definition of the dual features that we borrow from [15] relies on the assumption that each edge of the mesh to which a feature is assigned is shared by exactly two faces, hence implying edge-manifoldness. However, the assumption of edge-manifoldness of the input mesh is not required by PD-MeshNet for the convolution operation – which can handle an arbitrary number of neighbors – nor is necessary for the pooling operation – which does not alter the topological type of the mesh, as opposed, *e.g.*, to the *edge collapse* used in [15] (cf. [23] and Fig. C.1). Therefore, by simply adding nodes in the dual graph or changing the definition of features, PD-MeshNet can handle non-manifold edges. Considering the non-manifold edge shared by faces  $A$ ,  $B$  and  $C$  in Fig. C.2, we identify the following two possible solutions:

1. Two separate dual nodes  $\{A, B\}$  and  $\{A, C\}$  can be defined; since each is associated to exactly two faces (respectively  $A, B$  and  $A, C$ ), the same features as [15] (cf. Sec. 3.1 in the main paper) can be used.
2. A single dual node  $\{A, B, C\}$  can be inserted in the graph. In this case, different features need to be defined; one possibility is to concatenate – or average – the features that can be defined between faces  $A, B$  and faces  $A, C$  (cf. Sec. 3.1 in the main paper).

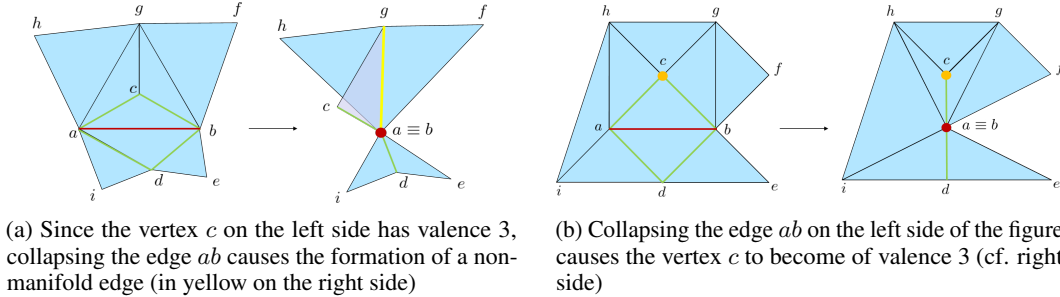


Figure C.1: The *edge collapse* operation used for pooling in [15] cannot collapse edges adjacent to valence-3 vertices, because it would break the assumption of edge-manifoldness required by the convolution operation of [15]; a valence-3 vertex is formed whenever an edge adjacent to a valence-4 vertex is collapsed. On the contrary, PD-MeshNet does not require edge-manifoldness to define its convolution operation, and its pooling operation does not alter the topological type of the mesh.

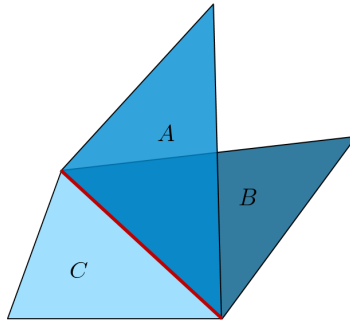


Figure C.2: Shown in red is an example of non-manifold edge shared by three faces  $A$ ,  $B$ , and  $C$ .

## C.2 Dual-graph features

We provide in the following a detail about the definition of the dual features. For each dual node  $\{A, B\}$  we replace the internal angles  $\gamma_A$  and  $\gamma_B$  used as features by [15] with the *edge-to-edge ratios* of the faces  $A$  and  $B$ , i.e., with reference to Fig. 2 in the main paper,  $\frac{\|ab\|}{\|ad\|}$ ,  $\frac{\|ab\|}{\|bd\|}$  and  $\frac{\|ab\|}{\|bc\|}$ ,  $\frac{\|ab\|}{\|ac\|}$  are used respectively in place of  $\gamma_A$  and  $\gamma_B$ . It should be noted that the two types of features encode the same type of information. Indeed, for instance by the law of cosines one has:

$$\begin{aligned} 2\|ad\|\|bd\|\cos(\gamma_A) &= \|ad\|^2 + \|bd\|^2 - \|ab\|^2 \Rightarrow \\ \Rightarrow 2\cos(\gamma_A) &= \frac{\|ad\|}{\|bd\|} + \frac{\|bd\|}{\|ad\|} - \frac{\|ab\|}{\|ad\|} \frac{\|ab\|}{\|bd\|} \Rightarrow \\ \Rightarrow \cos(\gamma_A) &= \frac{1}{2} \left( \frac{k_1}{k_2} + \frac{k_2}{k_1} - k_1 k_2 \right), \end{aligned} \quad (1)$$

with  $k_1 := \frac{\|ab\|}{\|ad\|}$  and  $k_2 := \frac{\|ab\|}{\|bd\|}$ .

## C.3 Dual-graph configurations

The following section introduces different possible configurations of the dual graph; the ablation study in Sec. C.4 shows that the choice of any of these configurations produces no significant differences in performance.

We define three admissible configurations of the dual graph, depending on whether a single or a double dual node is defined for each edge of the mesh, and on the directness of the edges of the dual graph:

**Single dual nodes.** For each pair of adjacent mesh faces  $A, B \in \mathcal{F}(\mathcal{M})$ , a *single* node  $\{A, B\}$  is inserted in the graph. This is the configuration introduced in the main paper, and we refer to it as *dual-graph configuration*  $\textcircled{A}$ . As previously mentioned, this is the configuration implicitly used by the method of Hanocka et al. [15], and for each dual node we therefore define the same features as [15], up to the implementation detail mentioned in Sec. C.2. In symbols, with reference to Fig. 2 in the main paper, one has the following feature vector for a generic dual node  $\{A, B\}$ :

$$\tilde{\mathbf{f}}_{\{A,B\}} = \left[ \theta_{AB}, \frac{\|ab\|}{h_A}, \frac{\|ab\|}{h_B}, \frac{\|ab\|}{\|ad\|}, \frac{\|ab\|}{\|bd\|}, \frac{\|ab\|}{\|bc\|}, \frac{\|ab\|}{\|ac\|} \right]^\top. \quad (2)$$

It should be noted that the both the edge-to-height ratios and the edge-to-edge ratios in (2) are defined up to rotational symmetry, i.e., one can have:

$$\tilde{\mathbf{f}}_{\{A,B\}} = \left[ \theta_{AB}, \frac{\|ab\|}{h_B}, \frac{\|ab\|}{h_A}, \frac{\|ab\|}{\|bc\|}, \frac{\|ab\|}{\|ac\|}, \frac{\|ab\|}{\|ad\|}, \frac{\|ab\|}{\|bd\|} \right]^\top \quad (3)$$

in alternative to (2). To solve the ordering ambiguity, similarly to [15] we further sort both the edge-to-height ratios and the edge-to-edge ratios in increasing order. Each edge in the graph is *undirected*, i.e., each node  $\{A, B\}$  is connected to its neighboring nodes  $\{A, M\}$ ,  $M \in \mathcal{N}_A \setminus \{B\}$  and  $\{B, N\}$ ,  $N \in \mathcal{N}_B \setminus \{A\}$  both with *incoming* (e.g.,  $\{A, M\} \rightarrow \{A, B\}$ ) and *outgoing* (e.g.,  $\{A, B\} \rightarrow \{A, M\}$ ) edges (Fig. C.3a).

**Double dual nodes.** Alternatively, one can map each pair of adjacent faces  $A, B \in \mathcal{F}(\mathcal{M})$  to a *double* dual node, by inserting a node  $A \rightarrow B$  and a node  $B \rightarrow A$  in the dual graph. This allows avoiding the symmetry ambiguity in the features: without loss of generality, we assign to the dual node  $A \rightarrow B$  the subset of the features in (2) that represent the geometry of face  $A$  as seen from face  $B$ , and to node  $B \rightarrow A$  the features that represent the geometry of face  $B$  as seen from face  $A$ , i.e., with reference to Fig. 2 in the main paper:

$$\tilde{\mathbf{f}}_{A \rightarrow B} = \left[ \theta_{AB}, \frac{\|ab\|}{h_A}, \frac{\|ab\|}{\|ad\|}, \frac{\|ab\|}{\|bd\|} \right]^\top, \quad \tilde{\mathbf{f}}_{B \rightarrow A} = \left[ \theta_{AB}, \frac{\|ab\|}{h_B}, \frac{\|ab\|}{\|bc\|}, \frac{\|ab\|}{\|ac\|} \right]^\top. \quad (4)$$

The edges in the graph can be both *undirected* and *directed*, i.e., a generic dual node  $A \rightarrow B$  can be connected to the neighboring nodes  $M \rightarrow A$ ,  $M \in \mathcal{N}_A \setminus \{B\}$  and  $B \rightarrow N$ ,  $N \in \mathcal{N}_B \setminus \{A\}$ :

- Both with an *incoming* and an *outgoing* edge, as done for generic graphs in [24] (where the neighboring nodes are instead of the form  $A \rightarrow M$  and  $N \rightarrow B$ ). We refer to this configuration as *dual-graph configuration*  $\textcircled{B}$  (Fig. C.3b);

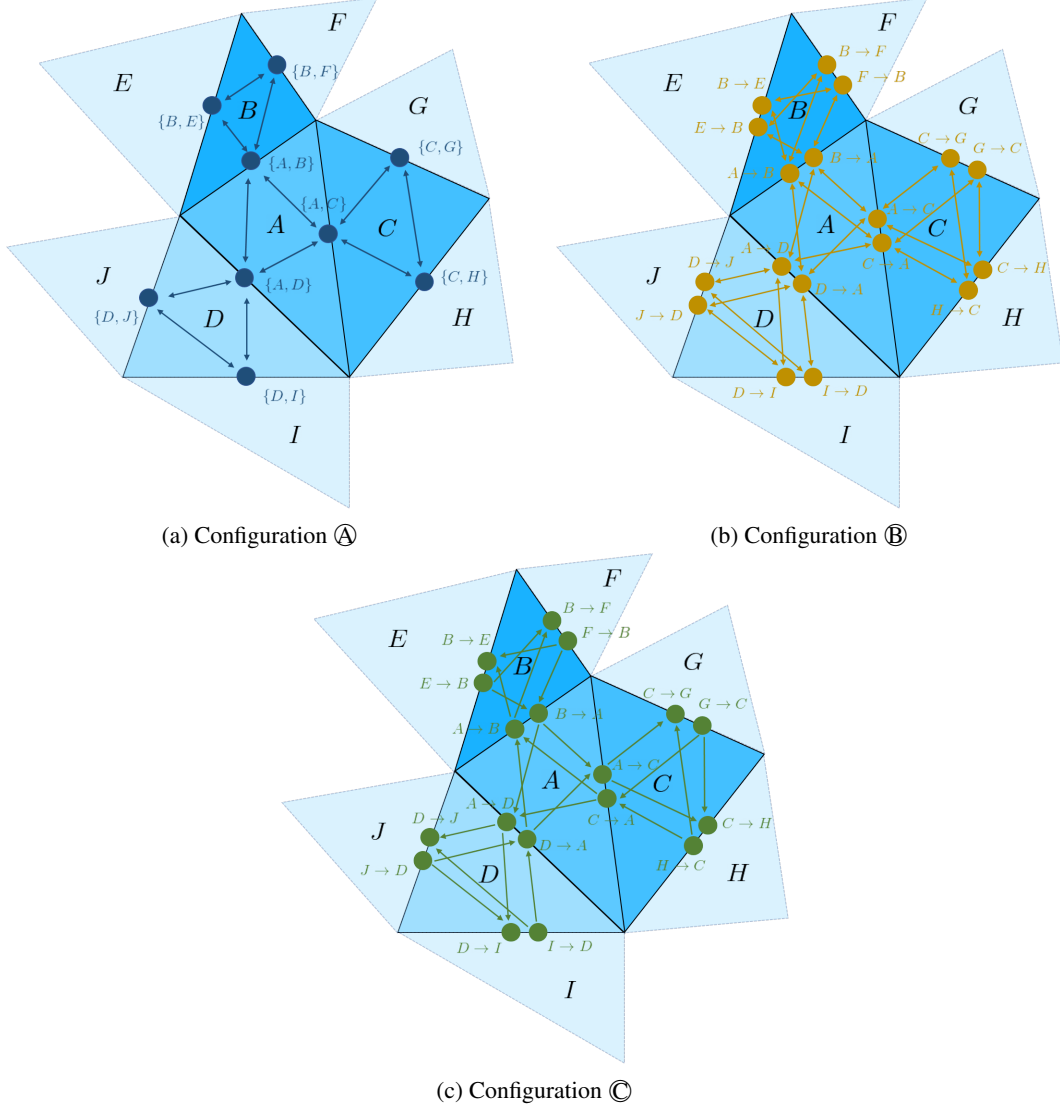


Figure C.3: Admissible dual-graph configurations for an example mesh.

- Only with edges outgoing from  $M \rightarrow A$  and incoming in  $B \rightarrow N$ , i.e., of the form  $(M \rightarrow A) \rightarrow (A \rightarrow B)$  and  $(A \rightarrow B) \rightarrow (B \rightarrow N)$ . We term this configuration *dual-graph configuration ③* (Fig. C.3c).

#### C.4 Ablation study

We experimentally noticed no substantial differences in performance across the three configurations, and in the main paper we therefore reported for simplicity the results obtained for dual-graph configuration ①. Below we present the results of an ablation study performed on the SHREC dataset for the mesh classification task and on the Human Body dataset for the mesh segmentation task, using for both the parameters provided in Sec. F. The training process is run for 200 epochs for the classification experiment and for 20 epochs (considering the whole augmented dataset) for the segmentation experiment. As shown in Tables C.2 and C.3, in the mesh segmentation task the single-node configuration (①) performs slightly better than the double-node configurations (② and ③), while the latter outperform configuration ① by a small margin in the mesh classification task.

Dual-graph configuration	Split 16	Split 10
Ⓐ	99.72%	99.11%
Ⓑ	<b>100.00%</b>	<b>99.78%</b>
Ⓒ	<b>100.00%</b>	99.67%

Table C.2: Classification accuracy on the SHREC dataset for the three admissible dual-graph configurations. Similarly to what done in the main paper, we limit the training to 200 epochs, and for each split we randomly generate 3 sets and average the results over these.

Dual-graph configuration	Face labels
Ⓐ	<b>84.78%</b>
Ⓑ	84.18%
Ⓒ	83.53%

Table C.3: Segmentation accuracy on the Human Body dataset for the three admissible dual-graph configurations. Similarly to what done in the main paper, we generate 20 augmented versions of each training sample by randomly sliding vertices along the mesh edges. Mean pooling aggregation is used.

## D Further details on convolution

In the following section, we provide the mathematical details of the convolution operation used by PD-MeshNet according to the different dual-graph configurations. We use the notation introduced in the main paper, and we further define the following symbols:

$\xi, \tilde{\xi}$	Non-linear activation functions (ReLU) associated with the primal and dual layer respectively
$W, \tilde{W}$	Shared learnable kernel used to multiply respectively primal- and dual- node features
$\eta, \tilde{\eta}$	Non-linear activation functions (Leaky-ReLU) used before softmax when computing primal- and dual- attention coefficients respectively
$a, \tilde{a}$	Learnable attention parameters used in the computation of the primal- and dual- attention coefficients respectively
$f_A    f_B$	Vertical concatenation between features $f_A$ and $f_B$

### D.1 Dual convolution

In the following, we assume  $(A, B)$  to be a pair of adjacent mesh faces. It should be noted that for each dual node the neighborhoods that index the summations in the equations in the section below match exactly those defined in the medial graph  $M(\mathcal{G}(\mathcal{M}))$  (cf. Fig. C.3 and Fig. 1c in the main paper); optionally, self-loops can be inserted in the graph, and multiple attention heads can be used, with the resulting features being either concatenated or averaged.

#### D.1.1 Dual-graph configuration Ⓐ

For the generic dual node  $\{A, B\}$ , the layer outputs the following feature:

$$\tilde{f}'_{\{A,B\}} = \tilde{\xi} \left( \sum_{M \in \mathcal{N}_A \setminus \{B\}} \tilde{\alpha}_{\{A,M\},\{A,B\}} \tilde{f}_{\{A,M\}} \tilde{W} + \sum_{N \in \mathcal{N}_B \setminus \{A\}} \tilde{\alpha}_{\{B,N\},\{A,B\}} \tilde{f}_{\{B,N\}} \tilde{W} \right). \quad (5)$$

The attention coefficient  $\tilde{\alpha}_{\{A,M\},\{A,B\}}$  defined on the generic dual edge  $\{A, M\} \rightarrow \{A, B\}$ , with  $M \in \mathcal{N}_A \setminus \{B\}$ , can be found as follows:

$$\tilde{\alpha}_{\{A,M\},\{A,B\}} = \frac{e^{\tilde{\eta}(\tilde{\mathbf{a}}^T[\tilde{\mathbf{f}}_{\{A,M\}}\tilde{\mathbf{W}}\|\tilde{\mathbf{f}}_{\{A,B\}}\tilde{\mathbf{W}}])}}{\sum_{K \in \mathcal{N}_A \setminus \{B\}} e^{\tilde{\eta}(\tilde{\mathbf{a}}^T[\tilde{\mathbf{f}}_{\{A,K\}}\tilde{\mathbf{W}}\|\tilde{\mathbf{f}}_{\{A,B\}}\tilde{\mathbf{W}}])}} + \sum_{N \in \mathcal{N}_B \setminus \{A\}} e^{\tilde{\eta}(\tilde{\mathbf{a}}^T[\tilde{\mathbf{f}}_{\{B,N\}}\tilde{\mathbf{W}}\|\tilde{\mathbf{f}}_{\{A,B\}}\tilde{\mathbf{W}}])}}. \quad (6)$$

Similarly, the attention coefficient  $\tilde{\alpha}_{\{B,N\},\{A,B\}}$  defined on the generic dual edge  $\{B, N\} \rightarrow \{A, B\}$ , with  $N \in \mathcal{N}_B \setminus \{A\}$ , can be computed as:

$$\tilde{\alpha}_{\{B,N\},\{A,B\}} = \frac{e^{\tilde{\eta}(\tilde{\mathbf{a}}^T[\tilde{\mathbf{f}}_{\{B,N\}}\tilde{\mathbf{W}}\|\tilde{\mathbf{f}}_{\{A,B\}}\tilde{\mathbf{W}}])}}{\sum_{M \in \mathcal{N}_A \setminus \{B\}} e^{\tilde{\eta}(\tilde{\mathbf{a}}^T[\tilde{\mathbf{f}}_{\{A,M\}}\tilde{\mathbf{W}}\|\tilde{\mathbf{f}}_{\{A,B\}}\tilde{\mathbf{W}}])}} + \sum_{K \in \mathcal{N}_B \setminus \{A\}} e^{\tilde{\eta}(\tilde{\mathbf{a}}^T[\tilde{\mathbf{f}}_{\{B,K\}}\tilde{\mathbf{W}}\|\tilde{\mathbf{f}}_{\{A,B\}}\tilde{\mathbf{W}}])}}. \quad (7)$$

### D.1.2 Dual-graph configuration ②

For the generic dual node  $A \rightarrow B$ , the layer outputs the following feature:

$$\tilde{\mathbf{f}}'_{A \rightarrow B} = \tilde{\xi} \left( \sum_{M \in \mathcal{N}_A \setminus \{B\}} \tilde{\alpha}_{M \rightarrow A, A \rightarrow B} \tilde{\mathbf{f}}_{M \rightarrow A} \tilde{\mathbf{W}} + \sum_{N \in \mathcal{N}_B \setminus \{A\}} \tilde{\alpha}_{B \rightarrow N, A \rightarrow B} \tilde{\mathbf{f}}_{B \rightarrow N} \tilde{\mathbf{W}} \right). \quad (8)$$

The attention coefficient  $\tilde{\alpha}_{M \rightarrow A, A \rightarrow B}$  defined on the generic dual edge  $(M \rightarrow A) \rightarrow (A \rightarrow B)$ , with  $M \in \mathcal{N}_A \setminus \{B\}$ , can be found as follows:

$$\tilde{\alpha}_{M \rightarrow A, A \rightarrow B} = \frac{e^{\tilde{\eta}(\tilde{\mathbf{a}}^T[\tilde{\mathbf{f}}_{M \rightarrow A} \tilde{\mathbf{W}}\|\tilde{\mathbf{f}}_{A \rightarrow B} \tilde{\mathbf{W}}])}}{\sum_{K \in \mathcal{N}_A \setminus \{B\}} e^{\tilde{\eta}(\tilde{\mathbf{a}}^T[\tilde{\mathbf{f}}_{K \rightarrow A} \tilde{\mathbf{W}}\|\tilde{\mathbf{f}}_{A \rightarrow B} \tilde{\mathbf{W}}])}} + \sum_{N \in \mathcal{N}_B \setminus \{A\}} e^{\tilde{\eta}(\tilde{\mathbf{a}}^T[\tilde{\mathbf{f}}_{B \rightarrow N} \tilde{\mathbf{W}}\|\tilde{\mathbf{f}}_{A \rightarrow B} \tilde{\mathbf{W}}])}}. \quad (9)$$

Similarly, the attention coefficient  $\tilde{\alpha}_{B \rightarrow N, A \rightarrow B}$  defined on the generic dual edge  $(B \rightarrow N) \rightarrow (A \rightarrow B)$ , with  $N \in \mathcal{N}_B \setminus \{A\}$ , can be computed as:

$$\tilde{\alpha}_{B \rightarrow N, A \rightarrow B} = \frac{e^{\tilde{\eta}(\tilde{\mathbf{a}}^T[\tilde{\mathbf{f}}_{B \rightarrow N} \tilde{\mathbf{W}}\|\tilde{\mathbf{f}}_{A \rightarrow B} \tilde{\mathbf{W}}])}}{\sum_{M \in \mathcal{N}_A \setminus \{B\}} e^{\tilde{\eta}(\tilde{\mathbf{a}}^T[\tilde{\mathbf{f}}_{M \rightarrow A} \tilde{\mathbf{W}}\|\tilde{\mathbf{f}}_{A \rightarrow B} \tilde{\mathbf{W}}])}} + \sum_{K \in \mathcal{N}_B \setminus \{A\}} e^{\tilde{\eta}(\tilde{\mathbf{a}}^T[\tilde{\mathbf{f}}_{B \rightarrow K} \tilde{\mathbf{W}}\|\tilde{\mathbf{f}}_{A \rightarrow B} \tilde{\mathbf{W}}])}}. \quad (10)$$

### D.1.3 Dual-graph configuration ③

For the generic dual node  $A \rightarrow B$ , the layer outputs the following feature:

$$\tilde{\mathbf{f}}'_{A \rightarrow B} = \tilde{\xi} \left( \sum_{M \in \mathcal{N}_A \setminus \{B\}} \tilde{\alpha}_{M \rightarrow A, A \rightarrow B} \tilde{\mathbf{f}}_{M \rightarrow A} \tilde{\mathbf{W}} \right). \quad (11)$$

The attention coefficient  $\tilde{\alpha}_{M \rightarrow A, A \rightarrow B}$  defined on the generic dual edge  $(M \rightarrow A) \rightarrow (A \rightarrow B)$ , with  $M \in \mathcal{N}_A \setminus \{B\}$ , can be found as follows:

$$\tilde{\alpha}_{M \rightarrow A, A \rightarrow B} = \frac{e^{\tilde{\eta}(\tilde{\mathbf{a}}^T[\tilde{\mathbf{f}}_{M \rightarrow A} \tilde{\mathbf{W}}\|\tilde{\mathbf{f}}_{A \rightarrow B} \tilde{\mathbf{W}}])}}{\sum_{K \in \mathcal{N}_A \setminus \{B\}} e^{\tilde{\eta}(\tilde{\mathbf{a}}^T[\tilde{\mathbf{f}}_{K \rightarrow A} \tilde{\mathbf{W}}\|\tilde{\mathbf{f}}_{A \rightarrow B} \tilde{\mathbf{W}}])}}. \quad (12)$$

## D.2 Primal convolution

For all dual-graph configurations, the output feature of a generic primal node  $A$  can simply be found as:

$$\mathbf{f}'_A = \xi \left( \sum_{M \in \mathcal{N}_A} \alpha_{M,A} \mathbf{f}_M \mathbf{W} \right). \quad (13)$$



What varies across the different dual-graph configurations is the attention coefficient  $\alpha_{M,A}$  associated to each generic primal edge  $M \rightarrow A$ , with  $M \in \mathcal{N}_A$ , as we detail below.

**Dual-graph configuration ①.**

$$\alpha_{M,A} = \frac{e^{\eta(\mathbf{a}^T \tilde{\mathbf{f}}'_{\{A,M\}})}}{\sum_{B \in \mathcal{N}_A} e^{\eta(\mathbf{a}^T \tilde{\mathbf{f}}'_{\{A,B\}})}}. \quad (14)$$

**Dual-graph configuration ② and ③.**

$$\alpha_{M,A} = \frac{e^{\eta(\mathbf{a}^T \tilde{\mathbf{f}}'_{M \rightarrow A})}}{\sum_{B \in \mathcal{N}_A} e^{\eta(\mathbf{a}^T \tilde{\mathbf{f}}'_{B \rightarrow A})}}. \quad (15)$$

## E Further details on pooling

### E.1 Implementation details

As shown in Sec. 3.3, contracting edges in the primal graph according to the quantity (1) in the main paper causes the formation of clusters of faces that belong in general to a triangle fan. One special case that can occur is the one in which a single primal edge not selected for contraction according to (1) from the main paper prevents the formation of a *closed* triangle fan. Consider the example of Fig. E.4: the edges between the pairs of faces  $(A, B)$ ,  $(B, E)$ ,  $(C, D)$ , and  $(D, E)$  are selected for contraction according to (1) from the main paper, but the one before faces  $A$  and  $C$  is not. As a consequence, one would have the formation of a new primal node (cluster of faces)  $ABCDE$  with a self-loop corresponding to the edge originally between primal nodes  $A$  and  $C$ . To avoid generating such self-loop, we force the single edge that prevents the formation of a *closed* triangle fan (between nodes  $A$  and  $C$  in the example) to also be collapsed.

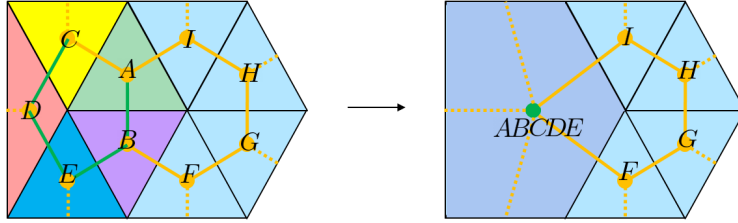


Figure E.4: Example of contraction of a primal edge performed even though the quantity (1) from the main paper is not among the largest  $K$ . The edges selected for contraction according to (1) from the main paper are shown in green on the left side. The primal edge between faces  $A$  and  $C$  is also contracted because it is the only one that prevents the faces  $A, B, C, D$  and  $E$  from forming a *closed* triangle fan after pooling.

## F Architectures and training details

### F.1 Classification

The results reported for the classification experiments are obtained using the architecture shown in Fig. F.5, with input graphs of dual-graph configuration ①, and using 3 attention heads with concatenation of the output features across the different heads. Each residual convolutional block contains two stacked convolutional layers with a single skip connection and each followed by group normalization (GN) [25] and ReLU activation. The network is trained for 200 epochs using cross-entropy loss and a fixed learning rate of  $2e-4$ . A batch size of 16 is used. A summary of the architecture parameters can be found in Tab. F.4.



Module type	#in channels (primal/dual)	#out channels (primal/dual)	Fract. primal edges pooled
Conv+GN+ReLU	1 / 7	$64 * H / 64 * H$	–
SC+Conv+GN+ReLU	$64 * H / 64 * H$	$64 * H / 64 * H$	–
Pooling	–	–	0.2
Conv+GN+ReLU	$64 * H / 64 * H$	$128 * H / 128 * H$	–
SC+Conv+GN+ReLU	$128 * H / 128 * H$	$128 * H / 128 * H$	–
Pooling	–	–	0.2
Avg pool	$128 * H / 128 * H$	$- / 128 * H$	–
Linear	$- / 128 * H$	$- / 100$	–
Linear	$- / 100$	$- / C$	–

Table F.4: Parameters of the architecture used for the classification experiments (cf Fig. F.5).  $H$  denotes the number of attention heads (3 in our experiments), while  $C$  is the number of classes in the dataset (30 for the SHREC dataset, 22 for the Cube Engraving dataset).  $SC$  indicates a skip connection from the previous module.

the attention heads and concatenated to the feature outputted by the unpooling layer. The second convolutional layer in each decoder level returns the output for the subsequent decoder level. A final convolutional layer predicts per-class labels for each class of the input mesh. We use 3 attention heads in each convolutional block of the encoder and 1 in each block of the decoder. We train the network for 1000 epochs with a learning rate of  $1e-3$  using cross-entropy loss on the per-face class labels. We use a batch size of 16 for the COSEG experiments and a batch size of 12 for the experiments on the Human Body dataset.

A summary of the architecture parameters can be found in Tab. F.5.

Level	Level type	Module type	#in channels (primal/dual)	#out channels (primal/dual)	Fract. primal edges pooled
1	Encoder	Conv+GN+ReLU	1 / 7	$32 * H_e / 32 * H_e$	–
1	Encoder	SC.+Conv+GN+ReLU	$32 * H_e / 32 * H_e$	$32 * H_e / 32 * H_e$	–
1	Encoder	Pooling	–	–	0.3
2	Encoder	Conv+GN+ReLU	$32 * H_e / 32 * H_e$	$64 * H_e / 64 * H_e$	–
2	Encoder	SC.+Conv+GN+ReLU	$64 * H_e / 64 * H_e$	$64 * H_e / 64 * H_e$	–
2	Encoder	Pooling	–	–	0.3
3	Encoder	Conv+GN+ReLU	$64 * H_e / 64 * H_e$	$128 * H_e / 128 * H_e$	–
3	Encoder	SC.+Conv+GN+ReLU	$128 * H_e / 128 * H_e$	$128 * H_e / 128 * H_e$	–
3	Encoder	Pooling	–	–	0.3
4	Single Conv	Conv+BN+ReLU	$128 * H_e / 128 * H_e$	$256 * H_e / 256 * H_e$	–
4	Single Conv	Average att. heads	$256 * H_e / 256 * H_e$	$256 / 256$	–
3	Decoder	Conv+BN+ReLU	$256 / 256$	$128 / 128$	–
3	Decoder	Unpooling	–	–	0.3 (unpooling)
3	Decoder	SCE	$128 / 128$	$128 * 2 / 128 * 2$	–
3	Decoder	Conv+BN+ReLU	$256 / 256$	$128 / 128$	–
2	Decoder	Conv+BN+ReLU	$128 / 128$	$64 / 64$	–
2	Decoder	Unpooling	–	–	0.3 (unpooling)
2	Decoder	SCE	$64 / 64$	$64 * 2 / 64 * 2$	–
2	Decoder	Conv+BN+ReLU	$128 / 128$	$64 / 64$	–
1	Decoder	Conv+BN+ReLU	$64 / 64$	$32 / 32$	–
1	Decoder	Unpooling	–	–	0.3 (unpooling)
1	Decoder	SCE	$32 / 32$	$32 * 2 / 32 * 2$	–
1	Decoder	Conv+BN+ReLU	$64 / 64$	$32 / 32$	–
1	Final	Conv+BN	$32 / 32$	$C / -$	–

Table F.5: Parameters of the architecture used for the segmentation experiments (cf Fig. F.6).  $H_e$  denotes the number of attention heads in the encoder (3 in our experiments).  $C$  is the number of classes in the dataset (4 for the categories `aliens` and `vases` of the COSEG dataset, 3 for the category `chairs` of the COSEG dataset, 8 for the Human Body dataset).  $BN$  denotes batch normalization.  $SC$  indicates a skip connection from the previous module.  $SCE$  indicates a skip connection from the corresponding block in the encoder: the attention heads from the encoder are averaged and the feature is concatenated to the feature outputted by the decoder module. The attention heads are also averaged at the output of the single convolutional layer in Level 4.

### Superpixel-like segmentation

We evaluate our method on the mesh segmentation task using also an encoder-only, alternative architecture, that we detail in the following. PD-MeshNet naturally forms clusters of faces through its task-driven pooling operation; therefore, by learning to form clusters of faces that all have the same ground-truth class label, the network could in principle predict a single class label for each cluster rather than a separate label for each face in the mesh. This idea relates to the concept of *superpixels* used in the context of image segmentation. Superpixels are sets of contiguous pixels that share common characteristics and that can be used to segment an image, by assigning them a class label. Usually, superpixels are formed through a clustering algorithm [28] based on pixel intensities and are later classified using learning-based techniques, but some works [29] have demonstrated the possibility of training a neural network to both form clusters of pixels and predict their class labels, in an end-to-end fashion. Similarly, we train PD-MeshNet to concurrently form clusters of faces – using its task-driven pooling operation – and label them, in an end-to-end fashion. We perform a small ablation study of this alternative method on the COSEG dataset. Fig. F.7 shows the *superpixel-like* architecture that we use in our additional evaluation. An encoder, made of 5 stacked residual convolutional blocks each with a single internal skip connection and each followed by a pooling layer, reduces the resolution of the input mesh by identifying face clusters (the mesh equivalent of superpixels in images). A final residual convolutional block predicts a class label for each cluster. The network is trained for 1000 epochs, using a fixed learning rate of  $1e-3$  and optimizing a cross-entropy loss function computed on the labels of each of the faces of the input mesh. These are retrieved from the labels predicted on the face clusters by simply mapping each face of the input mesh to its corresponding cluster in the output mesh. Each convolutional block uses 3 attention heads; for the experiments on the *aliens* and *vases* categories, we contract 10% of the primal edges in each pooling layer, while for the *chairs* category we set the fraction of primal edges to contract to 5%. Dual-graph configuration  $\textcircled{A}$  is used. As shown in Tab. F.6,

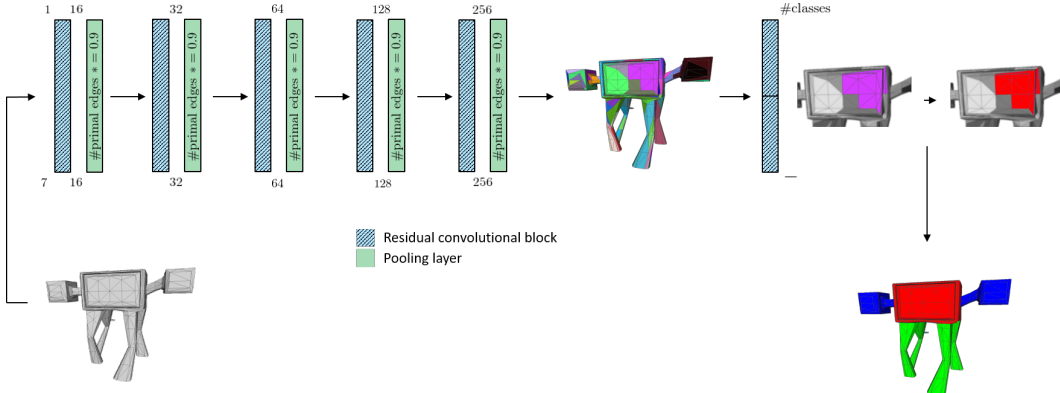


Figure F.7: Superpixel-like architecture used for segmentation. An encoder, made of a series of stacked residual convolutional blocks each followed by a pooling layer, identifies clusters of faces in the input mesh (example from the COSEG dataset [27]). A final convolutional block assigns a class label to each cluster. The label of each face in the original mesh can be retrieved as the label of the corresponding cluster.

the accuracy on the test set is slightly inferior ( $\sim 2.7\%$  to  $\sim 3.3\%$ ) to the one obtained using the U-Net architecture (cf. Tab. 3 in the main paper). We believe that this difference in performance w.r.t. the U-Net architecture can be attributed to: (i) the lack of skip connections between the different blocks, (ii) more importantly, to the difficulty of the network in forming face clusters by contracting a predefined number of primal edges, without any auxiliary supervision on the formation of clusters. Possible future directions include adding an auxiliary loss to guide the formation of the clusters, incorporating skip connections between the blocks of the architecture, and investigating more flexible approaches w.r.t. the number of primal edges to collapse.

Category	Face-label accuracy
aliens	94.75%
chairs	93.74%
vases	92.79%

Table F.6: Segmentation accuracy on the COSEG test dataset using the *superpixel-like* architecture.

## G Ablation study on components

In the following, we evaluate the contribution of the components of our method by performing an ablation study. We use the Humany Body dataset with the same network parameters as the experiments from the main paper (cf. previous section), and train for 300 epochs, without data augmentation.

Table G.7 shows the result of the experiments. When pooling is removed, taking away the convolution on the dual graph (*Primal-only no Pool*) worsens performance by  $\sim 31\%$  w.r.t. doing primal-dual convolution (*Ours no Pool*). Adding pooling significantly increases performance (by 6.74%, cf. *Ours mean*). We ablate the reduction function of the pooling layer and notice a small performance improvement when changing the aggregation from mean to sum (*Ours add*); for a more extensive evaluation of the influence of this factor, please cf. also Tab. H.8, which reports a comparison according also the edge-based labels.

Primal-only no Pool	Ours no Pool	Ours mean	Ours add
45.67%	77.53%	84.27%	<b>84.52%</b>

Table G.7: Face-label accuracy on the Human Body dataset for the ablation study on the contributions of the network components.

Finally, we ablate the importance of the primal graph by removing pooling and predicting labels on dual nodes (mesh edges). Note that this accuracy is not comparable to the one in Tab. G.7. Using only the dual graph results in edge-label accuracy of 80.16%; on the other hand, adding the primal graph (while keeping the training/testing procedure still on edges) produces an accuracy of 80.39%.

## H Metrics

For completeness, we report below the accuracy obtained by our approach according to two segmentation metrics that the method of Hanocka et al. [15] can be evaluated on, and that are different from the one based on face labels. The metrics below both require to predict class labels on the edges; therefore, it should be stressed that the results obtained on PD-MeshNet are not fully comparable with those obtained by [15], since our method predicts labels on faces, and the latter can at most be converted to *soft* labels on the edges, as shown in Fig. H.8. We denote the class label predicted on a generic mesh face  $A$  as  $l_A$ , and the soft label of the edge between two generic adjacent mesh faces  $A$  and  $B$  as  $l_{\{A,B\},\text{soft}}$ . Since in an edge-manifold mesh each non-boundary edge is shared by exactly two faces, the soft label of the edge between two faces  $A$  and  $B$  can be expressed as a pair, with its element being the labels of the two faces  $A$  and  $B$ , i.e.,  $l_{\{A,B\},\text{soft}} = (l_A, l_B)$ .

**Accuracy based on ground-truth edge *hard* labels.** This is the metric denoted as *Edge labels* in the main paper, and simply consists in evaluating the percentage of edges whose predicted label coincides with its single (*hard*) ground-truth label. Denoting the set of edges of a generic mesh  $\mathcal{M}$  as  $\mathcal{E}(\mathcal{M})$ , the ground-truth label of a generic edge  $\{A, B\} \in \mathcal{E}(\mathcal{M})$  as  $l_{\{A,B\}}^*$ , and its predicted class label as  $l_{\{A,B\}}$ , the accuracy can be found as:

$$\text{acc}_{\text{hard\_gt\_edge\_labels}} = \frac{\sum_{\{A,B\} \in \mathcal{E}(\mathcal{M})} \mathbb{I}[l_{\{A,B\}} = l_{\{A,B\}}^*]}{|\mathcal{E}(\mathcal{M})|} \cdot 100, \quad (16)$$

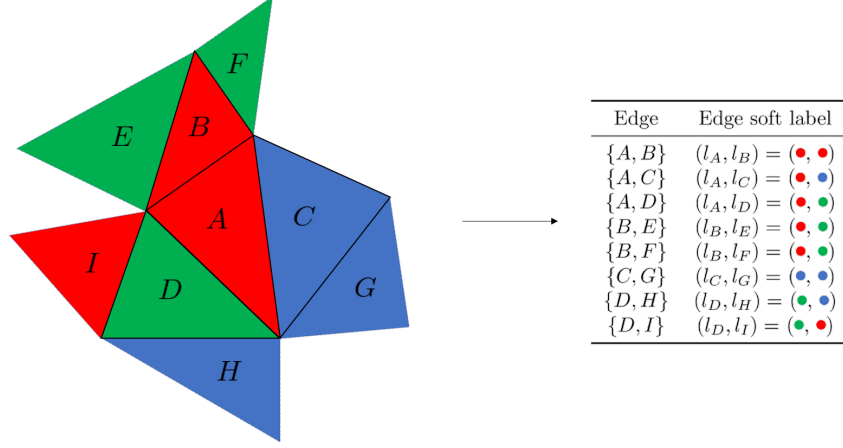


Figure H.8: Example conversion of face labels to edge soft labels. Assuming three possible class labels (corresponding to the red, green and blue colors on the left side), each edge is assigned a soft label by equally weighting the contributions of the two faces that share the edge (cf. right side).

where  $\llbracket \cdot \rrbracket$  denotes the Iverson bracket. Since, as detailed above, the predictions of our method can only be converted to *soft* edge labels, for our approach we evaluate the accuracy (16) by separately assuming for each edge  $\{A, B\} \in \mathcal{E}(\mathcal{M})$  the predicted *hard* label to coincide with the label predicted on the two faces  $A$  and  $B$ , and equally weighing the two contributions, *i.e.*,

$$\text{acc}_{\text{hard\_gt\_edge\_labels, ours}} = \frac{\sum_{\{A,B\} \in \mathcal{E}(\mathcal{M})} \left( 0.5 \cdot \llbracket l_A = l_{\{A,B\}}^* \rrbracket + 0.5 \cdot \llbracket l_B = l_{\{A,B\}}^* \rrbracket \right)}{|\mathcal{E}(\mathcal{M})|} \cdot 100. \quad (17)$$

**Accuracy based on ground-truth edge *soft* labels.** We further evaluate our method on the accuracy defined by [15]. This metric is based on ground-truth *soft* labels on the edges, and further weighs the contribution of each edge  $\{A, B\} \in \mathcal{E}(\mathcal{M})$  by its length, which we denote as  $\text{length}_{\{A,B\}}$ . We refer the reader to the official code of [15] for the exact implementation details; for our purposes, we will just consider the accuracy as being, for each edge  $\{A, B\}$ , a generic function  $f$  of the predicted *hard* label  $l_{\{A,B\}}$ , of the ground-truth *soft* label  $l_{\{A,B\},\text{soft}}^*$ , and of the edge length  $\text{length}_{\{A,B\}}$ . The metric can therefore be expressed as:

$$\text{acc}_{\text{soft\_gt\_edge\_labels}} = \frac{\sum_{\{A,B\} \in \mathcal{E}(\mathcal{M})} f\left(l_{\{A,B\}}, l_{\{A,B\},\text{soft}}^*, \text{length}_{\{A,B\}}\right)}{|\mathcal{E}(\mathcal{M})|} \cdot 100, \quad (18)$$

Similarly to (16), the problem with evaluating our method on the above metric is that the latter is a function, for each edge  $\{A, B\}$  of the ground-truth *hard* label  $l_{\{A,B\}}$ . Also in this case, we therefore separately assume  $l_{\{A,B\}}$  to coincide with the labels predicted on the two faces  $A$  and  $B$ , and we equally weigh the two contributions, *i.e.*,

$$\text{acc}_{\text{soft\_gt\_edge\_labels, ours}} = \frac{100}{|\mathcal{E}(\mathcal{M})|} \cdot \sum_{\{A,B\} \in \mathcal{E}(\mathcal{M})} \left[ 0.5 \cdot f\left(l_A, l_{\{A,B\},\text{soft}}^*, \text{length}_{\{A,B\}}\right) + 0.5 \cdot f\left(l_B, l_{\{A,B\},\text{soft}}^*, \text{length}_{\{A,B\}}\right) \right]. \quad (19)$$

For the computation of the accuracy, we use the official code and ground-truth soft labels provided by [15]. We run our experiments using dual-graph configuration **A** and the architecture detailed in Sec. F.2. Similarly to the main paper, we run each of the experiments of [15] 4 times – using the official code and parameters provided – and we report the best results obtained.



Dataset	Method	Metric		
		Edge labels (hard ground-truth)	Edge labels (soft ground-truth)	Face labels
COSEG aliens	MeshCNN [15]	95.35%	97.14%	96.26%
	Ours mean	96.51%	98.53%	97.63%
	Ours add	<b>97.06%</b>	<b>99.03%</b>	<b>98.18%</b>
COSEG chairs	MeshCNN [15]	92.65%	94.66%	92.99%
	Ours mean	96.26%	97.93%	97.08%
	Ours add	<b>96.44%</b>	<b>98.21%</b>	<b>97.23%</b>
COSEG vases	MeshCNN [15]	91.96%	96.91%	92.38%
	Ours mean	<b>94.70%</b>	<b>97.96%</b>	<b>95.47%</b>
	Ours add	94.57%	97.83%	95.36%
Human Body	MeshCNN [15]	84.05%	<b>92.05%</b>	85.39%
	Ours mean	84.13%	90.44%	84.78%
	Ours add	<b>85.09%</b>	91.11%	<b>85.61%</b>

Table H.8: Test accuracy on the mesh segmentation task according to the metrics defined in the paper. "Ours mean" and "Ours add" denote our method respectively with averaging and summation pooling aggregation, cf. Sec. 3.3 in the main paper.

## I Runtime

We perform our experiments using a single NVIDIA Quadro RTX 8000 GPU. Using the architectures detailed in Sec. F, one training epoch on the Split 16 of the SHREC dataset takes approximately 70s, while one training epoch on the *aliens* category of the COSEG dataset lasts for around 64s. The average time for a forward pass on a single mesh (*i.e.*, batch size 1) is  $\sim 175$ ms for the experiment on the SHREC dataset,  $\sim 390$ ms for the one on the COSEG *aliens* (1500 faces per mesh) dataset, and  $\sim 279$ ms for the experiments on the COSEG *chairs/vases* (1000 faces per mesh) dataset.

## References

- [1] J. Masci, D. Boscaini, M. M. Bronstein, and P. Vandergheynst, "Geodesic convolutional neural networks on Riemannian manifolds," in *Intl. Conf. on Computer Vision (ICCV)*, 2015.
- [2] D. Boscaini, J. Masci, E. Rodolà, and M. M. Bronstein, "Learning shape correspondence with anisotropic convolutional neural networks," in *Advances in Neural Information Processing Systems (NIPS)*, 2016.
- [3] F. Monti, D. Boscaini, J. Masci, E. Rodolà, J. Svoboda, and M. M. Bronstein, "Geometric deep learning on graphs and manifolds using mixture model CNNs," in *IEEE Conf. on Computer Vision and Pattern Recognition (CVPR)*, 2017.
- [4] N. Verma, E. Boyer, and J. Verbeek, "FeaStNet: Feature-Steered Graph Convolutions for 3D Shape Analysis," in *IEEE Conf. on Computer Vision and Pattern Recognition (CVPR)*, 2018.
- [5] I. S. Dhillon, Y. Guan, and K. Brian, "Weighted Graph Cuts without Eigenvectors: A Multilevel Approach," *IEEE Trans. Pattern Anal. Machine Intell.*, vol. 29, no. 11, pp. 1944–1957, 2007.
- [6] P. de Haan, M. Weiler, T. Cohen, and M. Welling, "Gauge Equivariant Mesh CNNs: Anisotropic convolutions on geometric graphs," *CoRR abs/2003.05425*, 2020.
- [7] J. Schult, F. Engelmann, T. Kontogianni, and B. Leibe, "DualConvMesh-Net: Joint Geodesic and Euclidean Convolutions on 3D Meshes," *CoRR abs/2004.01002*, 2020.
- [8] Y. Wang, Y. Sun, Z. Liu, S. E. Sarma, M. M. Bronstein, and J. M. Solomon, "Dynamic Graph CNN for Learning on Point Clouds," *ACM Trans. Graph.*, vol. 38, no. 5, p. 146, 2019.
- [9] M. Garland and P. S. Heckbert, "Surface Simplification using Quadric Error Metrics," in *ACM SIGGRAPH Intl. Conf. on Computer Graphics and Interactive Techniques (SIGGRAPH)*, 1997.
- [10] J. R. Rossignac and P. Borrel, "Multi-resolution 3D approximations for rendering complex scenes," *Modeling in Computer Graphics*, pp. 455–465, 1993.
- [11] I. Kostrikov, Z. Jiang, D. Panozzo, D. Zorin, and J. Bruna, "Surface Networks," in *IEEE Conf. on Computer Vision and Pattern Recognition (CVPR)*, 2018.

- [12] A. Ranjan, T. Bolkart, S. Sanyal, and M. J. Black, “Generating 3D faces using Convolutional Mesh Autoencoders,” in *European Conf. on Computer Vision (ECCV)*, 2018.
- [13] M. Tatarchenko, J. Park, V. Koltun, and Q.-Y. Zhou, “Tangent Convolutions for Dense Prediction in 3D,” in *IEEE Conf. on Computer Vision and Pattern Recognition (CVPR)*, 2018.
- [14] J. Huang, H. Zhang, L. Yi, T. Funkhouser, M. Niessner, and L. J. Guibas, “TextureNet: Consistent Local Parametrizations for Learning From High-Resolution Signals on Meshes,” in *IEEE Conf. on Computer Vision and Pattern Recognition (CVPR)*, 2019.
- [15] R. Hanocka, A. Hertz, N. Fish, R. Giryes, S. Fleishman, and D. Cohen-Or, “MeshCNN: A Network with an Edge,” *ACM Trans. Graph.*, vol. 38, no. 4, p. 90, 2019.
- [16] Y. Feng, Y. Feng, H. You, X. Zhao, and Y. Gao, “MeshNet: Mesh Neural Network for 3D Shape Representation,” in *AAAI Conf. on Artificial Intelligence (AAAI)*, 2019.
- [17] L. Yi, H. Su, X. Guo, and L. Guibas, “SyncSpecCNN: Synchronized Spectral CNN for 3D Shape Segmentation,” in *IEEE Conf. on Computer Vision and Pattern Recognition (CVPR)*, 2017.
- [18] S. Gong, L. Chen, M. Bronstein, and S. Zafeiriou, “SpiralNet++: A Fast and Highly Efficient Mesh Convolution Operation,” 2019.
- [19] J. L. Gross and J. Yellen, *Handbook of Graph Theory*. CRC Press, 2003.
- [20] B. Bollobas, *Modern Graph Theory*. Springer, 2013, ch. X, p. 368.
- [21] O. Ore, Ed., *The four-color problem*, ser. Pure and Applied Mathematics. Academic Press, 1967, vol. 27, ch. 9, p. 126.
- [22] H. Delingette, “Simplex Meshes: a General Representation for 3D Shape Reconstruction,” INRIA, Tech. Rep. 2214, Mar 1994.
- [23] T. Dey, H. Edelsbrunner, S. Guha, and D. V. Nekhayev, “Topology Preserving Edge Contraction,” *Publications de l’Institut Mathématique*, vol. 66, no. 80, pp. 23–45, 1999.
- [24] F. Monti, O. Shchur, A. Bojchevski, O. Litany, S. Günnemann, and M. M. Bronstein, “Dual-Primal Graph Convolutional Networks,” in *European Conf. on Machine Learning and Principles and Practice of Knowledge Discovery in Databases (ECML-PKDD)*, 2018.
- [25] Y. Wu and K. He, “Group Normalization,” in *European Conf. on Computer Vision (ECCV)*, 2018.
- [26] Z. Lian, A. Godil, B. Bustos, M. Daoudi, J. Hermans, S. Kawamura, Y. Kurita, G. Lavoua, H. Nguyen, R. Ohbuchi, Y. Ohikita, Y. Ohishi, F. Porikli, M. Reuter, I. Sipiran, D. Smeets, P. Suetens, H. Tabia, and D. Vandermeulen, “Shape Retrieval on Non-rigid 3D Watertight Meshes,” in *Eurographics Workshop on 3D Object Retrieval*, 2011.
- [27] Y. Wang, S. Asafi, O. van Kaick, H. Zhang, D. Cohen-Or, and B. Chen, “Active co-analysis of a set of shapes,” *ACM Trans. Graph.*, vol. 31, no. 6, p. 165, 2012.
- [28] R. Achanta, A. Shaji, K. Smith, A. Lucchi, P. Fua, and S. Süsstrunk, “SLIC Superpixels,” *IEEE Trans. Pattern Anal. Machine Intell.*, vol. 34, no. 11, pp. 2274–2282, 2012.
- [29] V. Jampani, D. Sun, M.-Y. Liu, M.-H. Yang, and J. Kautz, “Superpixel Sampling Networks,” in *European Conf. on Computer Vision (ECCV)*, 2018.